



Numerical simulation of an oscillating water column device using a code based on Navier–Stokes equations



Paulo R.F. Teixeira ^{a,*}, Djavan P. Davyt ^a, Eric Didier ^{b,c,d}, Rubén Ramalhais ^c

^a Universidade Federal do Rio Grande, Escola de Engenharia, Av. Itália, km 8, Campus Carreiros, 96201-900 Rio Grande, RS, Brazil

^b Laboratório Nacional de Engenharia Civil – LNEC, Departamento de Hidráulica e Ambiente, Av. do Brasil, 101, 1700-066 Lisboa, Portugal

^c Universidade Nova de Lisboa, Faculdade de Ciências e Tecnologia – FCT-UNL, 2829-516 Monte de Caparica, Portugal

^d MARETEC, Instituto Superior Técnico, Av. Rovisco Pais, 1049-001 Lisboa, Portugal

ARTICLE INFO

Article history:

Received 8 April 2013

Received in revised form

29 July 2013

Accepted 31 August 2013

Available online 29 September 2013

Keywords:

Numerical simulation

Finite element method

Wave energy

Oscillating water column

Turbine model

ABSTRACT

The study of ways of converting ocean wave energy into a useful one and the improvement of the existing equipment are complex engineering problems and very important issues in today's society. In this paper, the onshore oscillating water column device, in a 10 m deep channel subjected to 1 m high incident wave and wave periods from 4 s to 15 s, is investigated. The numerical analyses are carried out using Fluinco model that deals with incompressible flow problems based on the Navier–Stokes equations and employs the two-step semi-implicit Taylor–Galerkin method. An aerodynamic model is implemented in the algorithm to determine the air pressure that is imposed on the free surface. Analyses are divided into two sections. In the first section, the flow variables obtained by Fluinco and the commercial model Fluent are compared and similar results are obtained. In the second section, an investigation of the chamber geometry and turbine characteristic relation that provide the best device performance is carried out. In this case, variations in the front wall depth, the chamber length, the turbine characteristic relation and the chamber height, are made.

© 2013 Elsevier Ltd. All rights reserved.

1. Introduction

The potential of wave energy along coastal areas is a particularly attractive option in regions of high latitude. Along the coasts of northern Europe, North America, New Zealand, Chile and Argentina, for example, high densities of annual average wave energy are found (typically between 40 and 100 kW/m wave front) [1]. Nowadays, the possibility to extract this type of energy has become a reality. Therefore, several studies have been developed to assess and characterize wave energy resources in coastal zones accurately [2–6].

The OWC (oscillating water column) device has been studied since the 1940's, with Yoshio Masuda, who is considered the father of wave energy conversion technology [7]. However, development of technology for exploitation of wave energy to produce electricity on large scale began in the mid-1970's, when the first oil crisis occurred. Large multidisciplinary knowledge exists in technology to transform energy contained in sea waves. Currently, there are

several proposed concepts and technologies for the extraction of wave energy at different stages of development. However, investigations are still in search for new proposals, since none of them can be considered the most appropriate and efficient yet [8]. Basically, two criteria can be used to classify systems for extraction of wave energy: location of the installation and method of energy conversion [9,10]. In the first criterion, devices are grouped into three classes: shoreline, near-shore and offshore. In the second one, systems are classified in OWC (oscillating water column), oscillating bodies (point absorbers or surging devices) and overtopping devices.

One of the first devices to capture wave energy developed and installed on the shoreline was an OWC. Essentially, this equipment consists of a chamber with an opening in communication with the sea and another with the atmosphere. Through the action of waves, free surface inside the chamber oscillates and causes displacement in the air above free surface. Then air is forced to flow through an air-duct where a turbine generates electricity. Energy to be captured is stronger where wave periods are close to the natural period of water column device.

The first prototype of such system was developed onshore at the end of the 80's, for example in Toftehallen, Norway (500 kW); Sakata, Japan (60 kW); Pico, Portugal (400 kW); Limpet, Scotland

* Corresponding author. Tel.: +55 53 32336922.

E-mail addresses: pauloteixeira@furg.br, prfreetasteixeira@gmail.com (P.R.F. Teixeira).

Nomenclature			
B	chamber length	P_p	pneumatic power
c	sound speed	P_w	power of the incident wave
c_p	specific heat at constant pressure	$Q_t = (p-p_0)/kt$	air flow through the turbine
c_v	specific heat at constant volume	s	sloshing parameter
d	frontal wall depth	T_e	temperature
D	width of the chamber	T	period
e	internal specific energy	v_i	($i = 1,2,3$) fluid velocity components
g_i	($i = 1,2,3$) gravity acceleration components	$^{(s)}v_i$	($i = 1,2,3$) velocity components at the free surface
h	water depth	V	air volume inside the chamber
hc	height of the chamber in relation to the mean water level	\dot{V}	air volume rate inside the chamber
h_E	characteristic size of the element	w_i	($i = 1,2,3$) mesh velocity components
H	wave height	β	safety factor
H_0	incident wave height	$\gamma = c_p/c_v$	ratio of specific heats
k_c	thermal conductivity	Δt_E	time step of the element
$k = 2\pi/L$	wave number	η	free surface elevation
kt	turbine characteristic relation	θ	phase angle
L	wavelength	λ	volumetric viscosity coefficient
p	pressure	μ	shear viscosity coefficient
p_0	atmospheric pressure	ρ	specific mass
		τ_{ij}	($i, j = 1,2,3$) components of the deviatoric tensor
		ω	wave frequency

(500 kW); and more recently Mutriku, Spain (300 kW). Although coastal systems are easily accessed and do not need moorings, incident energy is lower compared to offshore systems, due to dissipative effects of breaking and bottom friction. Therefore, OWC floating type systems were developed by several companies such as in Mighty Whale (Japan), Energetech (Australia), OE Buoy (Ireland) and Sperboy (England).

Many efforts have been made to research the wave energy conversion efficiency and operating performance of the OWC system. McCormick [11] developed a theoretical analysis of the pneumatic wave energy conversion buoy assuming independence of the buoy heave motion and the motion of the water column within the center pipe. The rigid-body model concept was employed by researchers to predict performance of devices such as submerged cylinders [12–15]. A theoretical model of the hydrodynamics of a fixed OWC device was developed by Evans [16] by considering the internal free surface as a rigid weightless piston which allowed the application of the oscillating body theory. In this model, Evans ignored the spatial variation of the interior free surface and assumed the small width of the interior free surface by comparison with the incident wavelength. Afterward, Falcão and Sarmento [17], Evans [18] and Falnes and McIver [19] improved the rigid-body approach of an OWC by allowing the increase in pressure at the free surface and the possibility of a non-plane wave surface. Evans and Porter [20] used potential theory to consider a rectangular OWC in terms of the width of the interior chamber and submerged depth of the front wall, neglecting the viscous effects. This analytical model is robust for arbitrary incident wave frequencies and applicable to the calculation of impulse response functions for a time domain description of the device performance in random seas.

Several researchers also applied the BEM (boundary element method) to simulate the behavior of the OWC devices, mainly when the chamber dimensions are not small by comparison with the wavelength. For the fixed wave energy device with a harbor in front of the entrance of the water column, Count and Evans [21] developed a numerical solution which is based on the 3D boundary integral method outside the OWC device and matched, at the opening, to an eigenfunction expansion suitable for a rectangular

inner region. You [22] and You et al. [23] studied the topographic effect on wave power devices in nearshore zones by using a 3D BEM, in which the solution of Laplace's equation is used to express the velocity potential of the wave motion in the device region. Lee et al. [24] used low order 3D BEM to predict the response of an isolated OWC accounting for the appropriate interior free surface boundary condition. Following this work, Brito-Melo et al. [25] applied the direct approach to predict the hydrodynamic performance of an OWC device, where the dynamic boundary condition in the interior free surface is modified to account for the applied pressure in the chamber. In this case, the oscillating air pressure inside the chamber was solved as a radiation problem. Delauré and Lewis [26] discussed the accuracy of low order BEM and its suitability for efficient hydrodynamic modeling of generic bottom mounted OWC power plants. In the context of a boundary integral equation method, Clément [27] constructed a two-dimensional numerical wave tank comprising the canonical nonlinear free surface boundary condition. Moreover, Clément considered the influence of front wall depth, shape and thickness on the free oscillation of the interior free surface. Wang et al. [28] studied numerically the hydrodynamic performance of the OWC type shoreline-mounted wave-power device within linear wave theory by using a BEM based on the Wehausen and Laitone 3D shallow water Green's function. This study is particularly interesting as the authors validated numerical computations with experimental measurements and considered the topographical effects of bottom slope and water depth on the performance of an OWC. Lopes et al. [29] applied the commercial BEM code WAMIT [30] to analyze the incidence of regular waves on a piercing cylindrical duct, simulating a floating OWC. The authors compared the results with experimental and analytical ones obtained by Evans [16]. Josset and Clément [31] applied the low order BEM to efficient hydrodynamic modeling of generic bottom mounted OWC power plants to estimate the annual performance of the wave energy plant on Pico Island. Alves et al. [32] developed the numerical analysis of an axisymmetric floating OWC by using a BEM to account for the hydrodynamic interferences between the floater and the OWC. The radiation capabilities of the floater and the effect of a deeply submerged mass (rigidly connected to the floater) were found to be important in the matching

of the system dynamics to a representative incident wave frequency.

Recently, researchers have developed numerical models based on the RANS (Reynolds-Averaged-Navier–Stokes) and two-phase VoF (Volume of Fluid) equations to analyze the OWC devices. Horko [33] used the commercially available Fluent computational fluid dynamics flow solver to model a complete OWC system in a two dimensional numerical wave tank. The author investigated the effect of the front wall aperture shape on the hydrodynamic conversion efficiency. Liu et al. [34] applied Fluent commercial software to investigate the nozzle effects of the chamber-duct system on the relative amplitudes of the inner free water surface. Marjani et al. [35] predicted the pneumatic energy in the air chamber of an oscillating water column system by the Fluent code. Liu et al. [36] practically designed the integrated structure of caisson breakwater-OWC chamber by using a model based on the RANS and VoF equations. The numerical results were compared and validated by the corresponding experimental data. The effects of several incident wave conditions and shape parameters on the wave energy conversion efficiency and performance of integrated system were investigated. Liu et al. [37] presented a numerical simulation based on the two-phase VoF model embedded with the orifice and porous media modules to investigate the wave elevation, pressure variation inside the chamber and the air flow velocity in the duct.

The application of optimization algorithms to the hydrodynamic design of wave energy converters has already been addressed by some authors [38–40]. Those studies yielded optimal geometrical configurations for wave energy extraction under specific conditions by the use of genetic algorithms which were applied to two different pitching devices [38,39] and to a two-body heaving device [40].

Research of this type of problem is closer to reality when a model that considers the complete Navier–Stokes equations is used. Therefore, a numerical code, called Fluinco, based on semi-implicit two-step Taylor–Galerkin method [41] is employed to simulate the action of regular waves on an OWC. The model adopts a tetrahedral linear element, which has the advantage to adapt to areas of complex geometry and to be an element of good computational efficiency. An ALE (arbitrary lagrangian eulerian) formulation is used to enable the solution of problems involving both large relative movement between bodies and surfaces, and movements of free surface. The spatial velocity mesh distribution is such that distortion of elements is minimized by smoothing through the use of functions that consider the influence of the velocity of each node belonging to boundary surfaces.

An aerodynamic model, based on the first law of thermodynamics and ideal gas isentropic transformation applied in the air inside the chamber [31], was implemented in the algorithm to determine the air pressure that is imposed on the free surface. Therefore, the variation of the air volume along the time, promoted by the free surface movement in the OWC chamber, induces the turbine flow and variation of the pressure inside the chamber, characterizing a coupling between hydrodynamic and aerodynamic systems, such as is observed in prototype device.

The code was validated for some case studies by Teixeira et al. [42] and Teixeira and Fortes [43]. Specifically, validation of the Fluinco code was carried out in numerical simulations of a regular incident wave on a simplified offshore OWC device (partially submerged vertical tube of a small circular cross-section) and its accuracy in this type of problems was clearly shown by comparing numerical results with experimental ones and other numerical results obtained by Fluent code [44,45].

In this study, an onshore OWC subjected to an incident regular wave height, H_0 , of 1.0 m with a range of periods from 4 s to 15 s is analyzed. Studies of onshore OWC considering the aerodynamic-

hydrodynamic coupling is the main goal of this paper. Firstly, results of the Fluinco numerical code are compared with those obtained by the Fluent commercial code based on the finite volume method to discretize the Navier–Stokes equations and the VoF technique to consider air–water phases. Afterwards, the influence of the chamber geometry and the turbine characteristic relation on the device performance in terms of pneumatic power is investigated with Fluinco code.

A description of the equations and numerical methods used in the Fluinco numerical code are presented in Section 2. The description of the problems under investigation and the comparison between Fluinco and Fluent results for OWC with open chamber and chamber turbine are presented in Section 3. In Section 4, the influence of several geometric parameters and the turbine characteristic relation on the OWC device behavior is investigated by the Fluinco code. Finally, the principal conclusions of this study are summarized in Section 5.

2. Fluinco model

2.1. Governing equations for fluid flows

Mass conservation for slightly compressible fluids, assuming constant entropy, may be expressed by the following equation:

$$\frac{\partial \rho}{\partial t} = \frac{1}{c^2} \frac{\partial p}{\partial t} = -\frac{\partial U_i}{\partial x_i} \quad (i = 1, 2, 3) \quad (1)$$

where ρ is the specific mass, c is the sound speed, p is the pressure, $U_i = \rho v_i$ and v_i are the fluid velocity components.

Equations expressing both momentum and energy conservation in ALE description complete the governing equations of the fluid flow problem:

$$\frac{\partial U_i}{\partial t} + \frac{\partial f_{ij}}{\partial x_j} - \frac{\partial \tau_{ij}}{\partial x_j} + \frac{\partial p}{\partial x_i} = w_j \frac{\partial U_i}{\partial x_j} \quad (i, j = 1, 2, 3) \quad (2)$$

$$\begin{aligned} \frac{\partial (\rho e)}{\partial t} + \frac{\partial (\rho e v_i)}{\partial x_i} + \frac{\partial}{\partial x_i} (v_i p) - \frac{\partial}{\partial x_i} (\tau_{ij} v_j) - \frac{\partial}{\partial x_i} \left(k_c \frac{\partial T_e}{\partial x_j} \right) \\ = w_i \frac{\partial (\rho e)}{\partial x_i} \quad (i, j = 1, 2, 3) \end{aligned} \quad (3)$$

where w_i are the mesh velocity components, T_e is the temperature, e is the internal specific energy, k_c is the thermal conductivity, g_i are the gravity acceleration components and $f_{ij} = v_j U_i$. τ_{ij} are the components of the deviatoric tensor, given by:

$$\tau_{ij} = \mu \left(\frac{\partial v_i}{\partial x_j} + \frac{\partial v_j}{\partial x_i} \right) + \lambda \frac{\partial v_k}{\partial x_k} \delta_{ij} \quad (i, j = 1, 2, 3) \quad (4)$$

where μ and λ are the shear and volumetric viscosity coefficients, respectively, δ_{ij} is the Kronecker delta. Initial and boundary conditions must be added to Eqs. (1)–(3) in order to define the problem uniquely. In incompressible flows, the energy equation, Eq. (3), can be solved independently, after the field of velocities is computed.

2.2. Time and space discretizations

The variables U_i are discretized in time domain using a Taylor series expansion. In the first step, corresponding to the time interval $[t^n, t^{n+1/2}]$, U_i are given by the following expression [46]:

$$\begin{aligned}
 U_i^{n+1/2} &= U_i^n + \frac{\Delta t}{2} \frac{\partial U_i^n}{\partial t} \\
 &= U_i^n - \frac{\Delta t}{2} \left(\frac{\partial f_{ij}^n}{\partial x_j} - \frac{\partial \tau_{ij}^n}{\partial x_j} + \frac{\partial p^n}{\partial x_i} + \frac{1}{2} \frac{\partial \Delta p}{\partial x_i} - w_j^n \frac{\partial U_i^n}{\partial x_i} \right) \quad (i, j = 1, 2, 3)
 \end{aligned} \quad (5)$$

where $\Delta p = p^{n+1} - p^n$. Using

$$\tilde{U}_i^{n+1/2} = U_i^n - \frac{\Delta t}{2} \left(\frac{\partial f_{ij}^n}{\partial x_j} - \frac{\partial \tau_{ij}^n}{\partial x_j} + \frac{\partial p^n}{\partial x_i} - w_j^n \frac{\partial U_i^n}{\partial x_i} \right) \quad (i, j = 1, 2, 3) \quad (6)$$

Eq. (4) is given by the following expression:

$$U_i^{n+1/2} = \tilde{U}_i^{n+1/2} - \frac{\Delta t}{4} \frac{\partial \Delta p}{\partial x_i} \quad (i = 1, 2, 3) \quad (7)$$

By discretizing Eq. (1) in time and applying Eq. (6), the result is:

$$\begin{aligned}
 \Delta \rho &= \frac{1}{c^2} \Delta p = -\Delta t \frac{\partial U_i^{n+1/2}}{\partial x_i} \\
 &= -\Delta t \left[\frac{\partial \tilde{U}_i^{n+1/2}}{\partial x_i} - \frac{\Delta t}{4} \frac{\partial}{\partial x_i} \frac{\partial \Delta p}{\partial x_i} \right] \quad (i = 1, 2, 3)
 \end{aligned} \quad (8)$$

The second step is given by the following expression:

$$U_i^{n+1} = U_i^n + \Delta t \frac{\partial U_i^{n+1/2}}{\partial t} = U_i^n - \Delta t \left(\frac{\partial f_{ij}^{n+1/2}}{\partial x_j} - \frac{\partial \tau_{ij}^{n+1/2}}{\partial x_j} + \frac{\partial p^{n+1/2}}{\partial x_i} - w_j^{n+1/2} \frac{\partial U_i^{n+1/2}}{\partial x_i} \right) \quad (i, j = 1, 2, 3) \quad (9)$$

where $p^{n+1/2} = p^n + 1/2 \Delta p$.

After space discretization, the flow is analyzed by the following algorithm:

- determine $\tilde{U}_i^{n+1/2}$ with Eq. (6);
- determine Δp with Eq. (8) and calculate $p^{n+1} = p^n + \Delta p$;

- determine $U_i^{n+1/2}$ with Eq. (7); and
- determine U_i^{n+1} with Eq. (9).

The classical Galerkin weighted residual method is applied to the space discretization. In the variables at $t + \Delta t/2$ instant, a constant shape function \mathbf{P}_E is used, and in the variables at t and $t + \Delta t$, a linear shape function \mathbf{N} is employed. By applying this procedure to Eqs. (6)–(9), the following expressions in the matrix form are obtained [46]:

$$\Omega_E^{n+1/2} \tilde{\mathbf{U}}_i^{n+1/2} = \mathbf{C} \bar{\mathbf{U}}_i^n - \frac{\Delta t}{2} \left[\mathbf{L}_j (\bar{\mathbf{f}}_{ij}^n - \bar{\boldsymbol{\tau}}_{ij}^n) + \mathbf{L}_i \bar{\mathbf{p}}^n - \mathbf{T} \bar{\mathbf{U}}_i^n - \Omega_E^{n+1/2} \bar{\rho} \bar{\mathbf{g}}_i \right] \quad (10)$$

$$\left(\tilde{\mathbf{M}} + \frac{\Delta t^2}{4} \mathbf{H} \right) \Delta \bar{\mathbf{p}} = \Delta t \left(\mathbf{L}_i^T \tilde{\mathbf{U}}_i^{n+1/2} + \mathbf{f}_a \right) \quad (11)$$

$$\bar{\mathbf{U}}_i^{n+1/2} = \tilde{\mathbf{U}}_i^{n+1/2} - \frac{\Delta t}{4 \Omega_E} \mathbf{L}_i \Delta \bar{\mathbf{p}} \quad (12)$$

$$\begin{aligned}
 \mathbf{M}^{n+1} \bar{\mathbf{U}}_i^{n+1} &= \mathbf{M}^n \bar{\mathbf{U}}_i^n + \Delta t \left[\mathbf{L}_j^T (\bar{\mathbf{f}}_{ij}^{n+1/2} - \bar{\mathbf{w}}_{ij}^{n+1/2} \bar{\mathbf{U}}_{ij}^{n+1/2}) - \mathbf{Q}_j \bar{\boldsymbol{\tau}}_{ij}^n \right. \\
 &\quad \left. + \mathbf{Q}_i (\bar{\mathbf{p}}^n + \Delta \bar{\mathbf{p}}/2) + \mathbf{S}_{bi} - \mathbf{C}^T \bar{\mathbf{g}}_i \right]
 \end{aligned} \quad (13)$$

$$\begin{aligned}
 \Omega_E^{n+1/2} &= \int_{\Omega^{n+1/2}} \mathbf{P}_E^T \mathbf{P}_E d\Omega & \mathbf{C} &= \int_{\Omega^n} \mathbf{P}_E^T \mathbf{N} d\Omega & \mathbf{L}_i &= \int_{\Omega^n} \mathbf{P}_E^T \frac{\partial \mathbf{N}}{\partial x_i} d\Omega \\
 \mathbf{T} &= \int_{\Omega^n} \mathbf{P}_E^T \mathbf{N} \bar{\mathbf{w}}_i^n \frac{\partial \mathbf{N}}{\partial x_i} d\Omega & \tilde{\mathbf{M}} &= \int_{\Omega^{n+1/2}} \mathbf{N}^T \left(\frac{1}{c^2} \right) \mathbf{N} d\Omega & \mathbf{H} &= \int_{\Omega^{n+1/2}} \frac{\partial \mathbf{N}^T}{\partial x_i} \frac{\partial \mathbf{N}}{\partial x_i} d\Omega \\
 \mathbf{f}_a &= - \int_{\Gamma^{n+1/2}} \mathbf{N}^T \mathbf{P}_E \mathbf{n}_i \tilde{\mathbf{U}}_i^{n+1/2} d\Gamma + \frac{\Delta t}{4} \left(\int_{\Gamma^{n+1/2}} \mathbf{N}^T \frac{\partial \mathbf{N}}{\partial x_i} \mathbf{n}_i \Delta \bar{\mathbf{p}} d\Gamma \right) \\
 \mathbf{M}^n &= \int_{\Omega^n} \mathbf{N}^T \mathbf{N} d\Omega & \mathbf{Q}_i &= \int_{\Omega^n} \frac{\partial \mathbf{N}^T}{\partial x_i} \mathbf{N} d\Omega & \mathbf{M}^{n+1} &= \int_{\Omega^{n+1}} \mathbf{N}^T \mathbf{N} d\Omega \\
 \mathbf{S}_{bi} &= - \left(\int_{\Gamma^{n+1/2}} \mathbf{N}^T \mathbf{P}_E \mathbf{n}_j d\Gamma \right) (\bar{\mathbf{f}}_{ij}^{n+1/2} - \bar{\mathbf{w}}_{ij}^{n+1/2} \bar{\mathbf{U}}_i^{n+1/2})
 \end{aligned} \quad (14)$$

where variables with upper bars at n and $n+1$ instants indicate nodal values, while those at $n+1/2$ instant represent constant values in the element. The matrices and vectors from Eq. (10)–(13) are volume and surface integrals that were obtained by applying the classical Galerkin method. They are expressed by Ref. [46]:

Equation (10) is solved using the conjugated gradient method with diagonal pre-conditioning [47]. In Eq. (12), the consistent mass matrix is substituted by the lumped mass matrix, and then this equation is solved iteratively. The scheme is stable conditionally and must comply with the Courant stability condition [48], in which the local time step of each element E must satisfy the following expression

$$\Delta t_E \leq \beta h_E / |u| \quad (15)$$

where h_E is the characteristic size of the element (lowest element edge), β is the safety factor (0.25 has been adopted in this study) and u is the fluid velocity.

2.3. KFSBC (Kinematic free surface boundary condition)

The free surface is defined by the interface between two fluids, water and air, where atmospheric pressure is considered constant (generally the reference value is null). In this interface, the KFSBC (Kinematic free surface boundary condition) is imposed. By using the ALE formulation, it is expressed as [49]:

$$\frac{\partial \eta}{\partial t} + {}^{(s)}\mathbf{v}_i \frac{\partial \eta}{\partial x_i} = {}^{(s)}\mathbf{v}_3 \quad (i = 1, 2, 3) \quad (16)$$

where η is the free surface elevation, ${}^{(s)}\mathbf{v}_i$ are the velocity components at the free surface. The Eulerian formulation is used in the x and y directions (horizontal plane) while the ALE formulation is employed in the z or vertical direction.

The time discretization of KFSBC is carried out in the same way as the one for the momentum equations as presented before. After applying expansion in Taylor series, the expressions for η at $n+1/2$ (first step) and $n+1$ (second step) instants are obtained:

$$\eta^{n+1/2} = \eta^n + \frac{\Delta t}{2} \left({}^{(s)}\mathbf{v}_3 - {}^{(s)}\mathbf{v}_1 \frac{\partial \eta}{\partial x_1} - {}^{(s)}\mathbf{v}_2 \frac{\partial \eta}{\partial x_2} \right)^n \quad (17)$$

$$\eta^{n+1} = \eta^n + \Delta t \left({}^{(s)}\mathbf{v}_3 - {}^{(s)}\mathbf{v}_1 \frac{\partial \eta}{\partial x_1} - {}^{(s)}\mathbf{v}_2 \frac{\partial \eta}{\partial x_2} \right)^{n+1/2}$$

The triangular elements coincide with the face of the tetrahedral elements on the free surface. By adopting a linear triangular element and applying the Galerkin method to Eq. (16), these equations can be written as:

$$\int_{A^{n+1/2}} \mathbf{N}_s^T \mathbf{N}_s dA \bar{\eta}^{n+1/2} = \int_{A^n} \mathbf{N}_s^T \mathbf{N}_s dA \bar{\eta}^n + \frac{\Delta t}{2} \left(\int_{A^n} \mathbf{N}_s^T \mathbf{N}_s dA \bar{\mathbf{v}}_3^n - \int_{A^n} \mathbf{N}_s^T \mathbf{N}_s dA \left({}^{(s)}\bar{\mathbf{v}}_i \frac{\partial \eta}{\partial x_i} \right)^n \right) \quad (18)$$

$$\int_{A^{n+1}} \mathbf{N}_s^T \mathbf{N}_s dA \bar{\eta}^{n+1} = \int_{A^n} \mathbf{N}_s^T \mathbf{N}_s dA \bar{\eta}^n + \Delta t \left(\int_{A^{n+1/2}} \mathbf{N}_s^T \mathbf{N}_s dA \bar{\mathbf{v}}_3^{n+1/2} - \int_{A^{n+1/2}} \mathbf{N}_s^T \mathbf{N}_s dA \left({}^{(s)}\bar{\mathbf{v}}_i \frac{\partial \eta}{\partial x_i} \right)^{n+1/2} \right)$$

where $i = (1, 2)$, A is the triangular element area, \mathbf{N}_s is the linear shape function, $\bar{\eta}^n$, $\bar{\eta}^{n+1/2}$ and $\bar{\eta}^{n+1}$ are nodal values of elevations at t , $t + \Delta t/2$ and $t + \Delta t$ instants, respectively. Equation (18) is solved in an iterative form in the same way as in the momentum equations.

2.4. Mesh movement

The mesh velocity vertical component w_3 is computed to diminish element distortions, keeping prescribed velocities on

moving (free surface) and stationary (bottom) boundary surfaces. The mesh movement algorithm adopted in this paper uses a smoothing procedure for the velocities based on these boundary surfaces. The updating of the mesh velocity at node i of the finite element domain is based on the mesh velocity of the nodes j that belong to the boundary surfaces, and is expressed in the following way [41]:

$$w_3^i = \sum_{j=1}^{ns} a_{ij} w_3^j / \sum_{j=1}^{ns} a_{ij} \quad (19)$$

where ns is the total number of nodes belonging to the boundary surfaces and a_{ij} are the influence coefficients between the node i inside the domain and the node j on the boundary surface given by the following expression:

$$a_{ij} = 1/d_{ij}^4 \quad (20)$$

with d_{ij} being the distance between nodes i and j . In other words, a_{ij} represents the weight that every node j on the boundary surface has on the value of the mesh velocity at nodes i inside the domain. When d_{ij} is low, a_{ij} has a high value, favoring the influence of nodes i , located closer to the boundary surface containing node j .

The free surface elevation, the mesh velocity and the vertical coordinate are updated according to the following steps:

- (1) Calculate $\eta^{n+1/2}$ and $\bar{U}_i^{n+1/2}$, Eq. (17) and Eq. (6), respectively.
- (2) Calculate Δp , Eq. (8).
- (3) Calculate $U_i^{n+1/2}$, Eq. (7).
- (4) Calculate U_i^{n+1} , Eq. (9).
- (5) Calculate η^{n+1} , Eq. (17).
- (6) Update the mesh velocity w_3 and the vertical coordinate x_3 :
 - (6.1) Calculate the mesh velocity in the free surface at $t + \Delta t$: ${}^{(s)}w_3^{n+1} = (\eta^{n+1} - \eta^n) / \Delta t$.
 - (6.2) Calculate the mesh velocity in the interior of the domain at $n+1$ e $n+1/2$ by using Eq. (19) and $w_3^{n+1/2} = (w_3^{n+1} + w_3^n) / 2$, respectively.
 - (6.3) Update the vertical coordinates in the interior of the domain: $x_3^{n+1/2} = x_3^n + w_3^n (\Delta t / 2)$, $x_3^{n+1} = x_3^n + w_3^{n+1/2} \Delta t$.

2.5. Aerodynamic model

The aerodynamic and hydrodynamic phenomena in the interior of the chamber are strongly coupled. The aerodynamic model implemented in the Fluinco code uses the methodology presented by Josset and Clément [31] that proposed an equation for the air pressure based on the first law of thermodynamics applied to the air column, considering the open system hypothesis and ideal gas. Assuming an isentropic transformation and kinetic and potential

energies negligible, the energy balance equation results in the following relation:

$$\frac{\dot{p}(t)}{p(t)} = \gamma \left[\frac{Q_t(t)}{V(t)} \left(1 - \varepsilon \frac{\rho(t) - \rho_0}{\rho(t)} \right) - \frac{\dot{V}(t)}{V(t)} \right] \quad (21)$$

where $Q_t = (p - p_0)/kt$ is air flow through the turbine; p e \dot{p} are pressure and its rate, respectively; p_0 is atmospheric pressure; V e \dot{V} are air volume inside the chamber and its rate, respectively; kt is the turbine characteristic relation; $\gamma = c_p/c_v$ (equal to 1.4 for the air), where c_p e c_v are specific heats at constant pressure and constant volume, respectively; ρ e ρ_0 are specific mass inside and outside the chamber, respectively; ε is null for negative value of air flow (air entering into the chamber) and one for opposite case. The relation between the air flow and the pressure drop across a Wells turbine is linear. Therefore, in this case, the turbine characteristic relation (kt) is assumed constant [50,51].

The compressibility effect is considered by the following relation of isentropic transformation:

$$p(t)\rho(t)^{-\gamma} = p_0\rho_0^{-\gamma} \quad (22)$$

In Fluinco code, Eq. (21) is discretized in time by using Taylor series up to second order. Therefore, the air pressure is updated in two steps through the following equations:

$$p^{n+1/2} = p^n + \frac{\Delta t}{2} \frac{\partial p^n}{\partial t} = p^n + \frac{\Delta t}{2} \left\{ \gamma p^n \left[-\frac{(p^n - p_0)}{kt V^n} \left(1 - \varepsilon \frac{\rho^n - \rho_0}{\rho^n} \right) - \frac{\dot{V}^n}{V^n} \right] \right\} \quad (23)$$

$$p^{n+1} = p^n + \Delta t \frac{\partial p^{n+1/2}}{\partial t} = p^n + \Delta t \left\{ \gamma p^{n+1/2} \left[-\frac{(p^{n+1/2} - p_0)}{kt V^{n+1/2}} \left(1 - \varepsilon \frac{\rho^{n+1/2} - \rho_0}{\rho^{n+1/2}} \right) - \frac{\dot{V}^{n+1/2}}{V^{n+1/2}} \right] \right\} \quad (24)$$

The flow rate \dot{V} is calculated multiplying the average vertical velocity of the nodes along the free surface inside the chamber by the area of the horizontal section of the chamber.

Equation (21) is discretized using also the same two step scheme, resulting the following equations for the specific mass:

$$\rho^{n+1/2} = \left(\frac{p_0}{p^n} \right)^{1/\gamma} \rho_0 \quad (25)$$

$$\rho^{n+1} = \left(\frac{p_0}{p^{n+1/2}} \right)^{1/\gamma} \rho_0 \quad (26)$$

The updated air pressure variation $\Delta p = p^{n+1} - p^n$, obtained through Eq. (24), is imposed as a boundary condition in the surface integral of \mathbf{f}_a term of Eq. (14) each time step.

3. Comparison between Fluinco and Fluent models

3.1. OWC with open chamber

The case study consists of a 10 m deep flume with a 10 m wide chamber at its end. The front wall submergence depth is set to 5 m and its thickness to 0.5 m. The length of the flume is fivefold the wavelength (L). The chamber is open to the atmosphere. Fig. 1 shows a sketch of the flume and chamber in the domain as

well as the gauge positions. One meter high waves with different periods ($T = 0.5$ s to 18 s) are simulated. The relation between the depth (h) and the wavelength (L) varies from 1/18 to 1/4, characterizing intermediate water depth. The relation between the wavelength (L) and the chamber length (B) ranges from 3.7 to 17.5.

In the Fluinco model, the domain is discretized by using tetrahedral elements in a regular mesh with 44 layers in the vertical direction, adopting high resolution (element sizes around 0.16 m) in free surface, bottom and submerged frontal wall of the chamber regions where large disturbance flow is expected. In the horizontal direction, the maximum element size is $L/50$. Element sizes are lower, around 0.1 m, near the frontal wall and inside the chamber. One layer of elements is used in the transversal direction, since the behavior of the flow is only 2D. The mesh node numbers used in the simulations ranged from 96,000 to 230,000 and the tetrahedral element numbers ranged from 235,000 to 560,000, according to the wave period case (lower values correspond to lower wave periods).

The time step is 0.0015 s, which satisfies the Courant condition. On the left side of the flume, the free surface elevation and the velocity components of the incident wave are imposed at each time instant according to the linear wave theory [52]. The slip condition is imposed on chamber and lateral walls and the no-slip condition is applied to the bottom.

Fluent numerical [53] code applies a finite volume technique to solve the continuity and the RANS equations. In this code, the variables are defined in the center of each control volume. The diffusive terms of the equations are discretized by the second order central difference scheme. The capture of the free surface is done by the VoF method [54]. The simulations are carried out with: the 2D/3D module of the code; implicit formulation; the second order time discretization; and the standard $k-\varepsilon$ turbulence model. The SIMPLEC algorithm is used for coupling pressure and velocity. Under-relaxation coefficients are equal to 1 for momentum and VoF but equal to 0.8 for $k-\varepsilon$. The convective terms in the faces of the control volumes, for the components of momentum, are determined by the MUSCL scheme, while second order upwind scheme is used for convective terms of k and ε equations. In the VoF method, the volume fraction on the faces of the control volumes is determined by a modified version of the HRIC (High Resolution Interface Capturing) scheme [55]. The pressure is determined by the PRESTO! (PREssure STaggering Option) scheme, classically used for wave propagation modeling in Fluent [53].

Previous studies have shown that wave propagation in Fluent is well simulated using 60 elements per wavelength and 20 elements in the region of the free surface [45,56]. Consequently, the mesh is constructed with 60 elements per wavelength, in the horizontal direction, with a refinement near the front wall edge. There are also 20 elements in the vertical direction in the free surface capture zone stretching from this zone and the bottom to the middle,

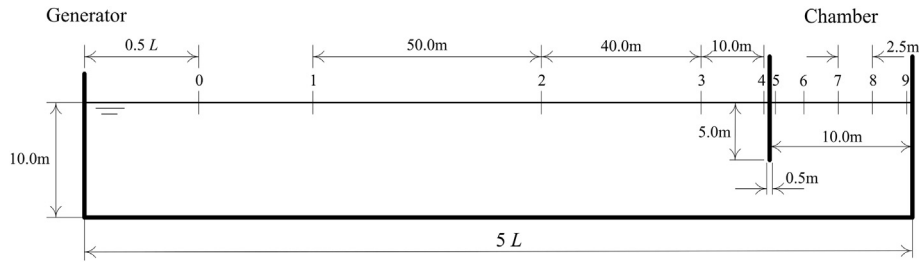


Fig. 1. Sketch of the domain and gauge positions for the OWC with open chamber.

totalizing around 41,000 quadrilateral elements for the different configurations (2D simulation for OWC with open chamber). Wave generation is simulated by imposing the velocity components and volume fraction (according to the free surface elevation along the time) on the boundary, both defined by the linear wave theory in intermediate water, such as in Fluinco code. A non-slip condition is imposed on the bottom, the front wall edge and the chamber walls. Finally, atmospheric pressure is imposed on the OWC chamber and the flume top. Time step is equal to $T/600$ and six non-linear iterations per time step enable to reduce the residue by at least two orders of magnitude which are enough for good accuracy in wave propagation simulation [56].

Comparisons among Fluinco and Fluent results are presented in this section. Fig. 2 shows the free surface elevation at the center of the chamber for 8 s and 10 s wave period. Results of both models are very close although some small differences in wave amplitude can be observed. The average differences of the extreme values

between Fluinco and Fluent results are -3.6% and $+1.3\%$, for $T = 8$ s and $T = 10$ s, respectively, considering Fluent values as reference.

Figs. 3 and 4 show streamlines and velocity modulus for waves of 7 and 12 s, respectively, at 8 instants along a time period. Disturbances of the flow near the front wall are found to be higher for the 7 s wave period, probably due to the fact that free surface elevations inside and outside the chamber are out of phase, as can be seen by the streamlines direction and the graph of the phase angles shown in Fig. 5. In both cases, some vortices, with no turbulence, are observed. Flow disturbances near the corner of the front wall also depend on the front wall shape; this influence was studied by researchers, such as Horko [33] and Morris-Thomas et al. [57].

Fig. 5 shows the amplification factor, defined as the ratio between the wave height inside the chamber (H) and the incident wave height (H_0), and the phase angle (θ), which is the angular difference between the wave inside and outside the chamber. Due to sloshing inside the chamber, a mean water elevation taken among the inner gauges is used for the computation of the amplification factor. Below the 7 s wave period, the amplification factor is lower than 1.0; above this value, the amplification rises up to about 15 s and then seems to stabilize. Good agreement between both models can be seen, with minor differences around 6% for wave periods of 10 s and 15 s. Concerning the phase angle, both curves show the same general characteristics. It can be observed that the phase angles are smaller (below 30° for Fluinco and 45° for Fluent, 33.3% difference) for higher periods (above 10 s). In this range, amplification factors are higher (between 2 and 2.3) whereas, for periods below 10 s, the angle phase increases, reaching 187° and 199° for Fluinco and Fluent (6.4% difference), respectively, and $T = 5$ s, and amplification factors decrease up to 0.3 for this wave period.

Fig. 6 shows the sloshing parameter (s), defined in this paper as the average of the maximum difference between the free surface elevation inside the chamber at the front wall minus the free surface elevation inside the chamber on the rear wall. A sloshing peak is found at 7 s, although Fluent model shows higher sloshing magnitude than Fluinco: $s = 0.65$ m and 0.5 m, respectively (23.1% difference). Nevertheless, the sloshing has the same behavior for the two codes. Minor values are found for periods above 11 s (around 0.1 m), in which the relation between the wavelength and the chamber length is almost 10 or above 10.

Sloshing phenomena can also be observed by studying the frequency spectrum of the free surface elevations inside the chamber. Fig. 7 shows the frequency spectrum of three gauges inside the chamber (front wall – gauge 5, middle – gauge 7, rear wall – gauge 9) for the 7 s and 12 s wave periods obtained by Fluinco. For wave period of 7 s, energy is concentrated in the fundamental frequency (incident wave frequency) on middle gauge 7, while a second component can be seen on front and rear wall gauges 5 and 9, indicating that sloshing occurs in the chamber. For wave period of 12 s, all gauges have almost the same spectrum, energy being concentrated almost solely in the fundamental frequency, which indicates the absence of sloshing in the chamber.

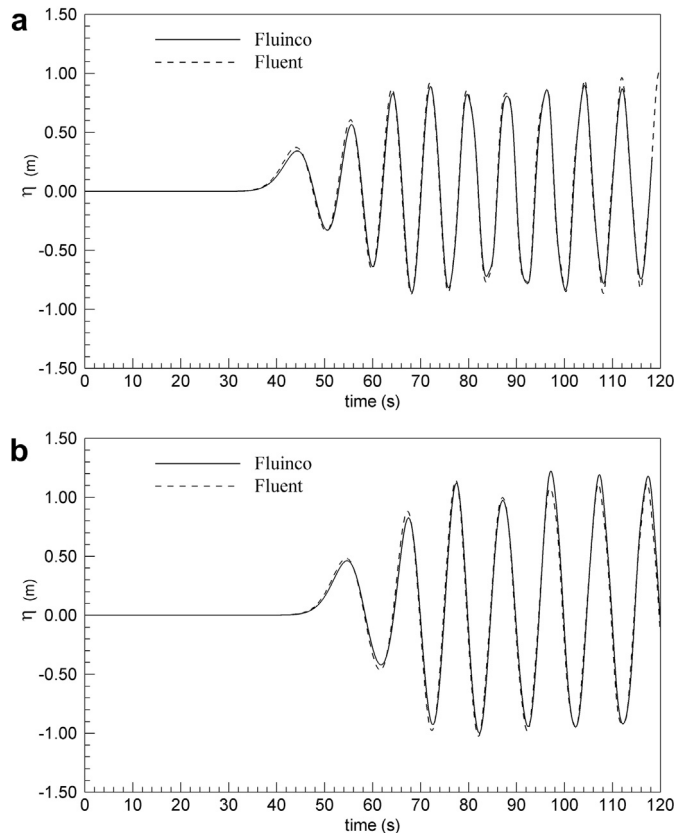


Fig. 2. Free surface elevations inside the chamber for the OWC with open chamber and (a) $T = 8$ s and (b) $T = 10$ s: comparison between Fluinco and Fluent.

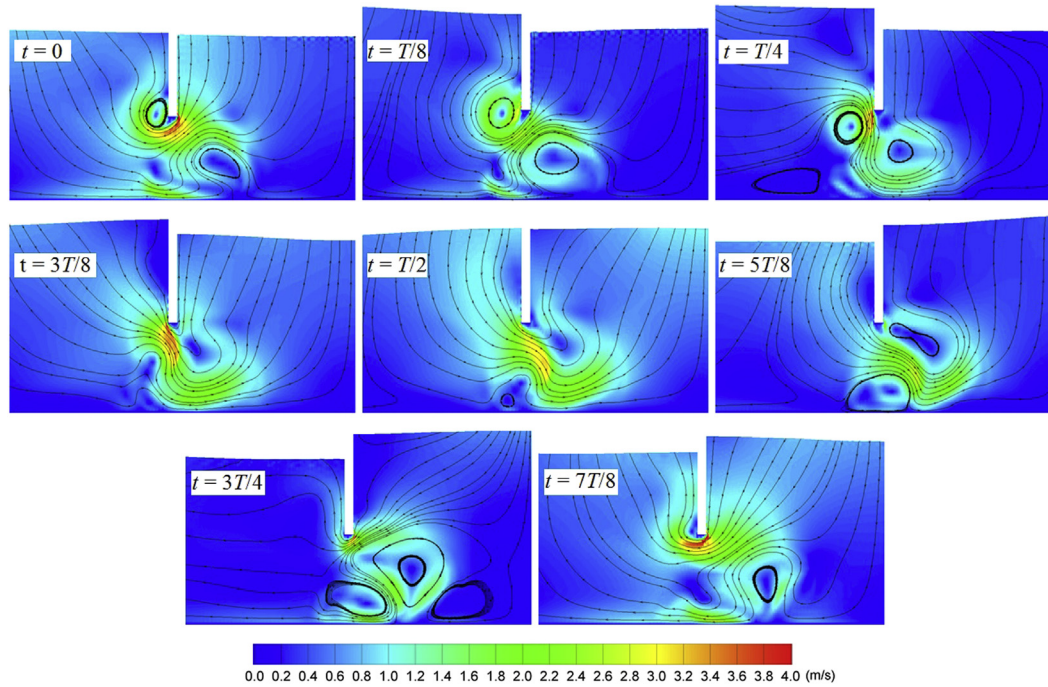


Fig. 3. Streamlines and velocity modulus for the OWC with open chamber and $T = 7$ s.

3.2. OWC with chamber turbine

The second study case, in which Fluinco and Fluent are compared, consists in a 10.0 m deep flume, whose length is five-fold the wavelength, and a 5.0 m long chamber (B) in its end, as shown in Fig. 8. The frontal wall is 0.5 m thick and $d = 5.0$ m deep. The width of the chamber is $D = 8.0$ m and the height in relation to the mean water level is $hc = 10.0$ m. A Wells turbine is considered

with a characteristic relation equal to $kt = 120 \text{ Pa m}^{-3} \text{ s}$, which is very similar to the one used in the European pilot plant built on the Pico island, Azores (Portugal) ($kt = 119.4 \text{ Pa m}^{-3} \text{ s}$) [50]. Incident regular waves with periods from 5.0 s to 12.0 s and 1.0 m high are simulated. Air-duct diameter is 1.0 m and its axis is located 8.5 m above the free surface at rest.

In the Fluinco model, the same discretization and boundary conditions of the OWC with open chamber case, described in

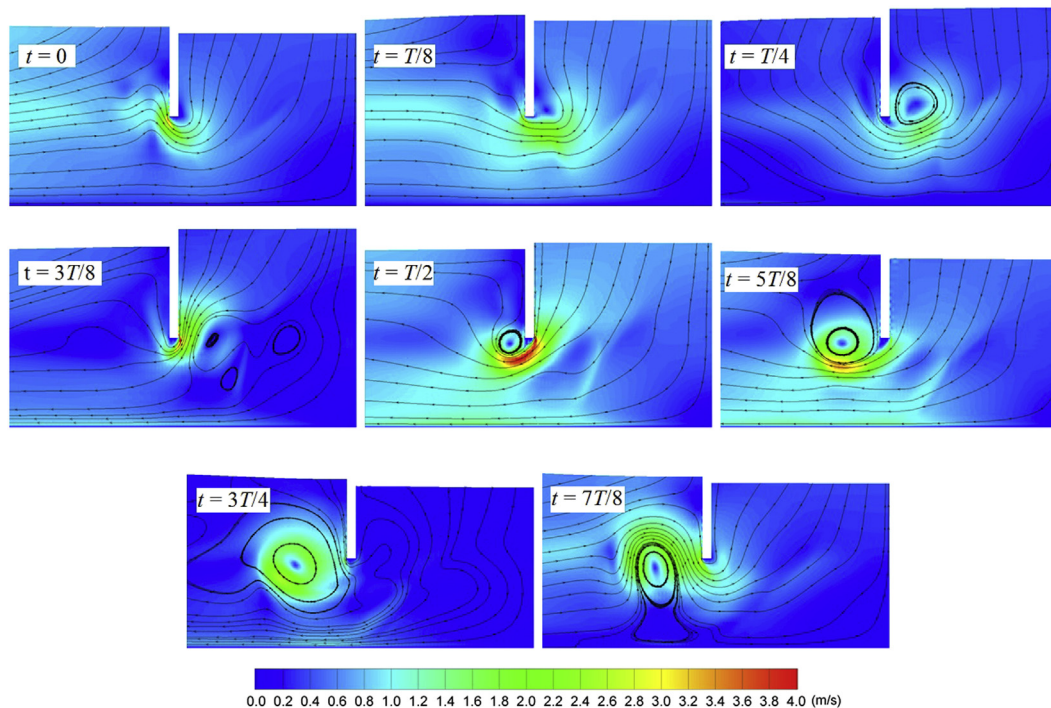


Fig. 4. Streamlines and velocity modulus for the OWC with open chamber and $T = 12$ s.

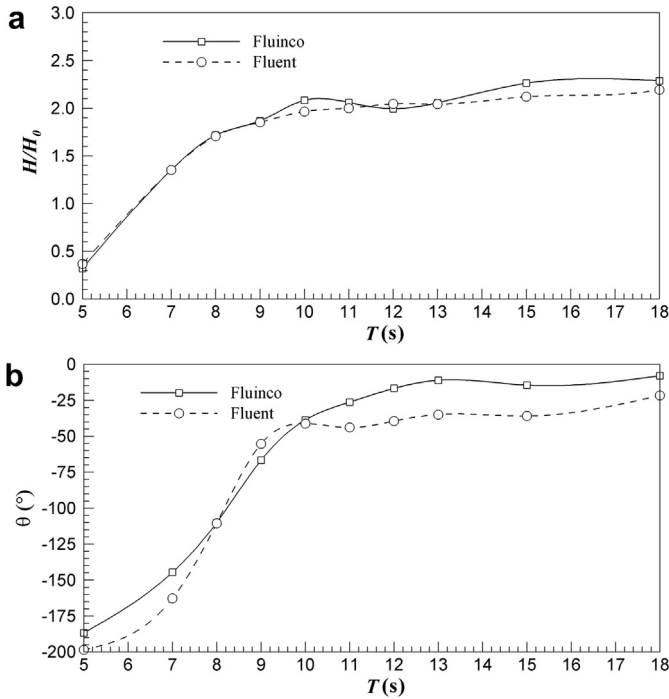


Fig. 5. Amplification factor (a) and phase angle (b) for the OWC with open chamber: comparison between Fluinco and Fluent.

Section 3.1, are used. The only difference is the imposition of the pressure on the free surface inside the chamber which is calculated according to the aerodynamic model presented in Section 2.5, taking into account the effect of the chamber dimension and the characteristic of the Wells turbine.

In Fluent model, the no-slip condition is imposed on the bottom and the device walls and the atmospheric pressure is imposed above the free surface, in the same way indicated in Section 3.1. At the end of the air-duct, located in the superior part of the chamber, the pressure drop caused by the turbine is imposed. The pressure drop is proportional to the flow rate according to the turbine characteristic relation. The 3D mesh used in this configuration is composed by a number of hexahedral and prismatic elements ranging from 261,848 to 330,240 according to the wave period case (lower values correspond to lower wave periods). The mesh discretization has the same characteristics as the one used in OWC with open chamber case [45].

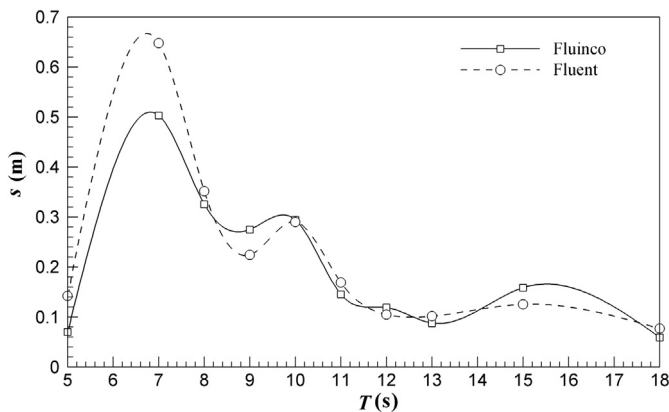


Fig. 6. Sloshing parameter for the OWC with open chamber: comparison between Fluinco and Fluent.

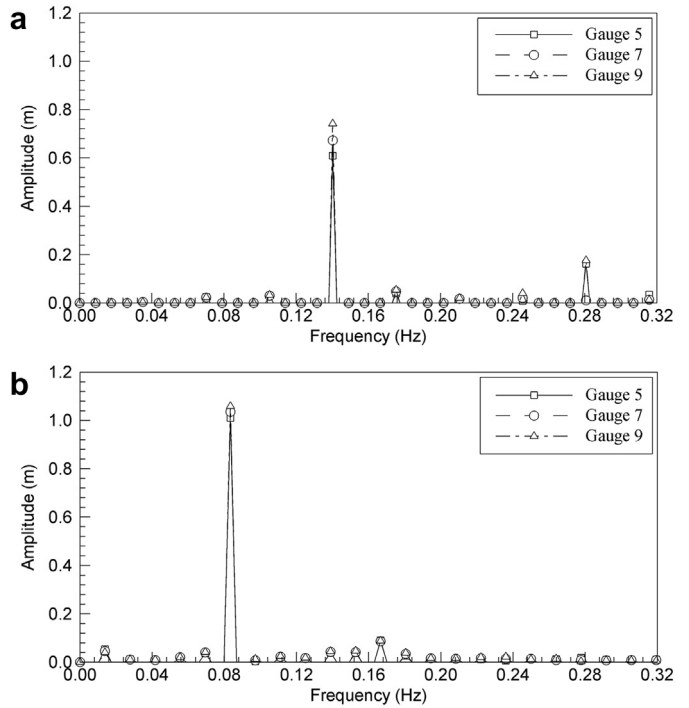


Fig. 7. Frequency spectrum obtained by Fluinco for gauges inside chamber for 7 s (a) and 12 s (b) wave period wave for the OWC with open chamber.

Figs. 9 and 10 show the typical mesh used in Fluinco and Fluent, respectively. In Fluinco, only the water domain is discretized since the numerical method is based on tracking free surface (the free surface is a boundary of the numerical domain). In Fluent, the mesh needs to be constructed in water and air domain (air chamber and air duct) since the numerical method is based on capturing method VoF to identify the free surface.

Fig. 11 shows the amplification factor and the phase angle obtained by Fluinco and Fluent. Both amplification factors are very similar and show the same trend, although, systematically, the ones obtained by Fluinco are slightly higher than those obtained by Fluent. Larger and smaller differences occurred in $T = 5$ s (26.84%) and $T = 12$ s (2.14%), respectively. When OWC is modeled with the turbine, it can be observed that the amplification factor increases with the wave period, without any optimum value in an intermediate zone. The phase angles obtained by Fluinco and Fluent are very similar with an average difference equal to 11.69%, without any systematic tendency to underestimation or overestimation of these results. It can be noticed that, the lower the phase angles are, the larger the amplification factors are. Between 5.0 s and 7.5 s, both phase angle and amplification factor show high variation.

Fig. 12 shows the sloshing parameter (s). It can be observed that, up to $T = 7.5$ s, the sloshing parameter is around 0.011 m (approximately 1% of the incident wave height). From this period to 12.0 s, the sloshing parameter decreases as the wave period increases, with a minimum value equal to 0.002 m at $T = 11.0$ s and high variations up to $T = 9.0$ s. In this range (from $T = 7.5$ – 9.0 s), there is the largest pneumatic power, as it can be noticed in Fig. 14.

Fig. 13 shows time series of the air pressure for periods of 5.0, 7.5, 9.0 and 12.0 s. For Fluent, the air pressure is monitored by four gauges and results shown in Fig. 13 correspond to their mean values. It can be observed that the air pressure frequencies are coincident with respective incident waves. Both models showed similar results. In the air entrance, Fluent model presents some disturbances in negative pressure, which is not noticed in the

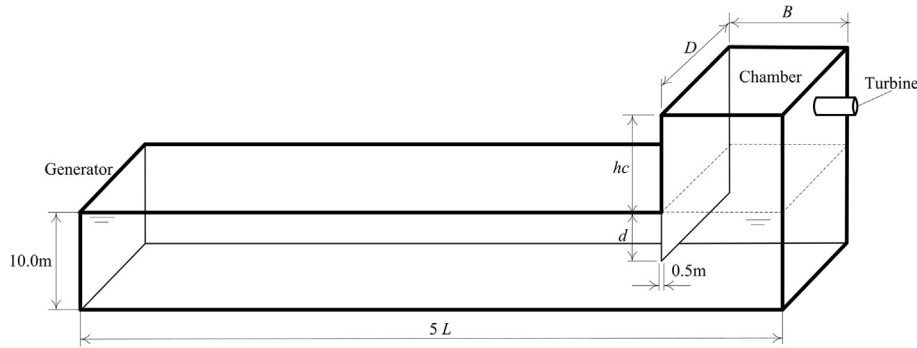


Fig. 8. Schematic representation of the flume and OWC with chamber turbine.

Fluinco model. These pressure disturbances do not destabilize the numerical solution and probably occur due to the geometric discontinuity caused by the tube. The largest difference between Fluinco and Fluent results occur at $T = 7.5$ s, where the positive amplitudes are approximately 3.2 kPa and 4.4 kPa, respectively (27.2% difference). Moreover, the lowest difference occurs at $T = 5.0$ s, where the positive amplitudes are approximately 2.2 kPa for both models.

Fig. 14 shows time series of the flow rate for periods of 5.0, 7.5, 9.0 and 12.0 s, comparing the results obtained for both models. Fluinco presents slightly higher values by comparison with those obtained by Fluent for periods of 5.0 s, 9.0 s and 12.0 s (differences in positive amplitudes of 25.9%, 14.1% and 31.2%, respectively), while for period of 7.5 s, the differences are lower (5.0% in positive amplitudes). Fluent presents non-symmetry between positive and negative values of flow rate, which do not appear in Fluinco results.

In this paper, the efficiency of the device is calculated by the relation between the pneumatic power, P_p , and the power of the correspondent incident wave, P_w . The pneumatic power is defined as the time-average of the product of the flow rate by the air pressure variation:

$$P_p = \frac{1}{T} \int_T Q_t (P - P_0) dt \quad (27)$$

Therefore, the pneumatic power is the one that is available for the turbine to generate mechanical power. The power of an incident wave is expressed as follows [52]:

$$P_w = \left(\frac{1}{8} \rho g H^2 \right) \frac{\omega}{k} \left[\frac{1}{2} \left(1 + \frac{2kh}{\sin h2kh} \right) \right] D \quad (28)$$

where g is the gravitational acceleration, H is the wave height, ω is the wave frequency, $k = 2\pi/L$ is the wave number, L is the wavelength and D is the chamber width.

Fig. 15 shows the efficiency of the device obtained by both models. It is observed that Fluinco and Fluent models present the same tendencies, although Fluent shows slightly higher values, mainly at 7.5 s (difference around 13%), where there is the highest power. These differences may have occurred due to different aerodynamic models, since the same differences are not observed in amplification factor and phase angle, which represent hydrodynamic parameters. While in Fluent model, the air pressure field is determined through the flow solution, in Fluinco model, it is obtained by using the first law thermodynamics, without taking into account the spatial distribution of the pressure inside the chamber. Fluid characteristic is different in Fluinco and Fluent: in Fluinco, air is compressible but it is not the case in Fluent where air is incompressible. Some researchers have studied the effects of compressibility on the performance of the OWC device. Thakker et al. [58], for example, showed that when using a compressible model, the efficiency is approximately 8% lower than the one in the case of the incompressible model. Nevertheless, the maximum power shown by both models is almost the same. The difference between Fluinco and Fluent for $T = 7.5$ s is about 13%, with a value of pneumatic power obtained by Fluinco slightly lower than that of Fluent, in good accordance with the results of Thakker et al. [58].

3.3. Discussion about the comparison between Fluinco and Fluent

Two numerical models, Fluinco and Fluent, both based on the Navier–Stokes equations, were applied to the very complex flow problem of interaction between an incident regular wave and an OWC device. Both codes are based on two very different numerical approaches for the discretization of equations, for free surface modeling and for aerodynamic simulation in the OWC chamber:

- Fluinco model is based on the finite element method. Only the water domain is discretized since the numerical method is

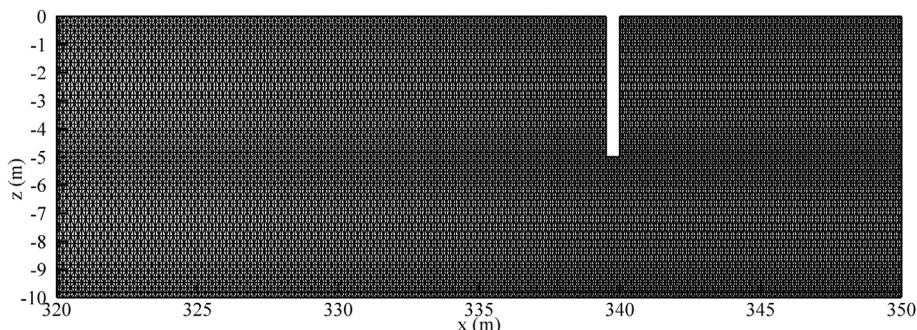


Fig. 9. Mesh used for Fluinco simulations.

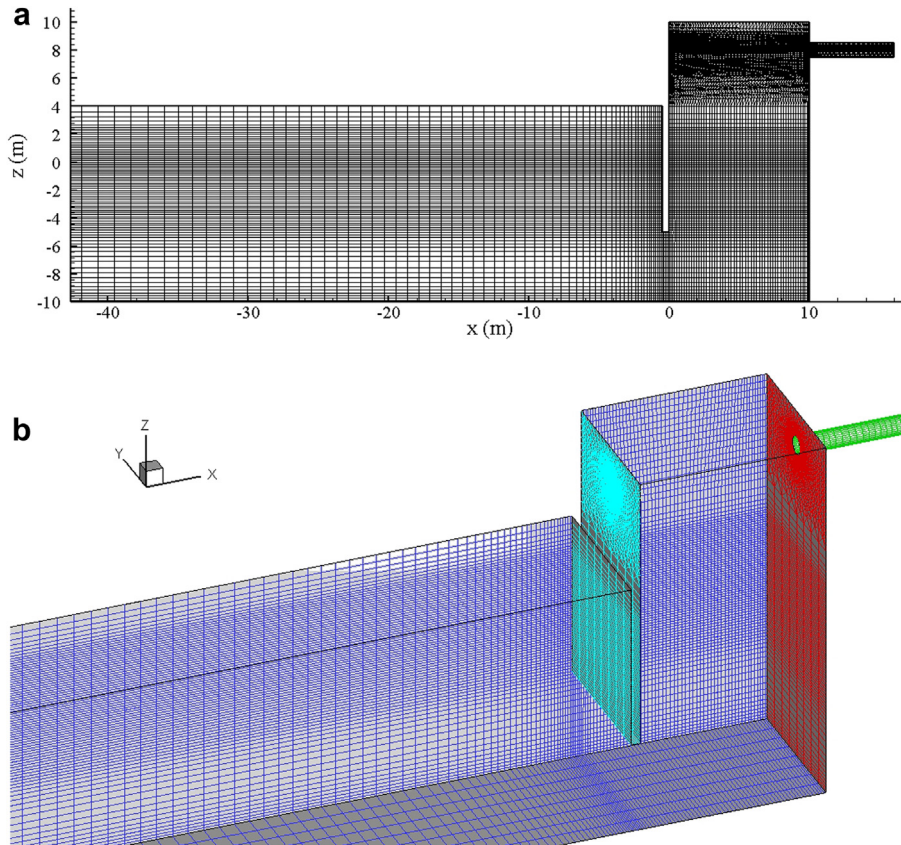


Fig. 10. Mesh used for Fluent simulations: (a) mesh on the vertical symmetric plane and (b) mesh on several boundaries.

based on tracking free surface (the free surface is a boundary of the numerical domain). Pressure in the chamber is calculated by an aerodynamic model which takes into account the effect of a Wells turbine. This model is based on an equation for the air

pressure deduced through the first law of thermodynamics applied to the air column, considering the open system hypothesis and ideal gas.

- Fluent model is based on the finite volume method. The mesh needs to be constructed in water and air domain (air chamber and air duct) since the numerical method is based on capturing method VoF to identify the free surface. Aerodynamics in the chamber is also simulated by solving RANS equations. The effect of Wells turbine is modeled using the characteristic relation of the turbine which relates the pressure loss to the flow rate in the air-duct where the turbine is located.

The results obtained by Fluinco and Fluent for two configurations of the OWC chamber, with open chamber and with chamber turbine, are in very good agreement in terms of free surface levels,

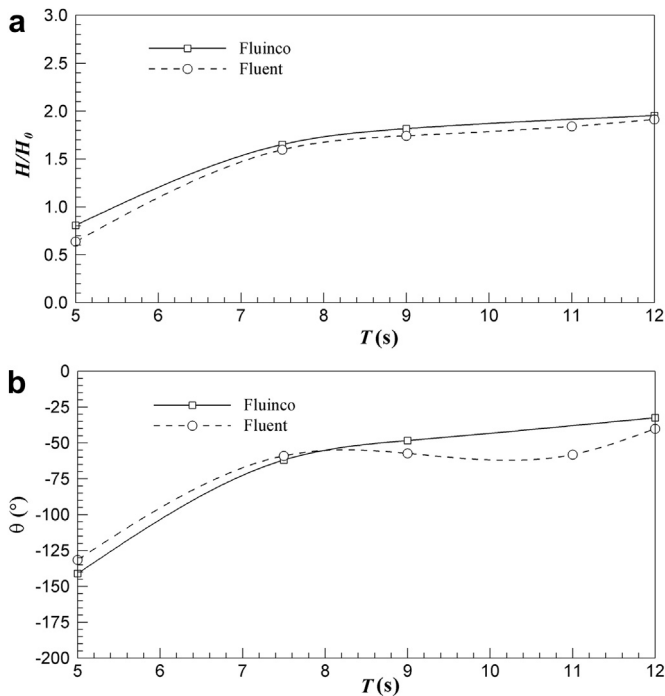


Fig. 11. Amplification factor (a) and phase angle (b) for the OWC with chamber turbine obtained by Fluinco and Fluent.

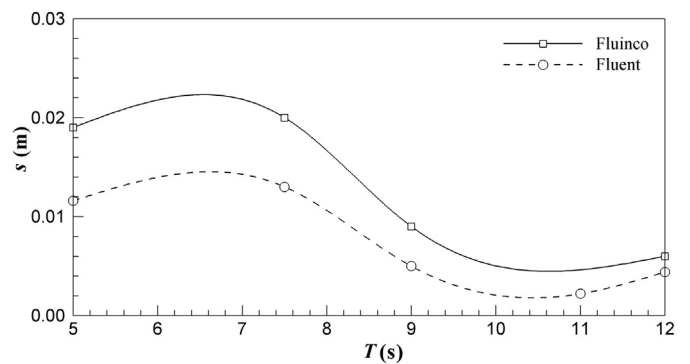


Fig. 12. Sloshing parameter for the OWC with chamber turbine obtained by Fluinco and Fluent.

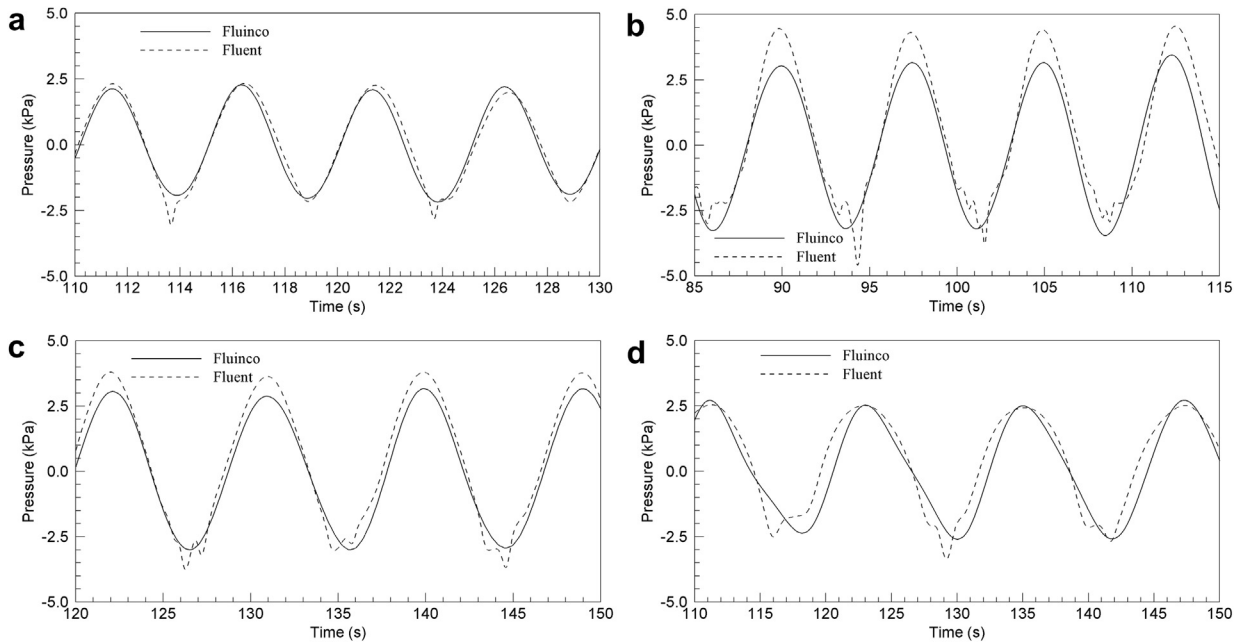


Fig. 13. Time series of air pressure inside the chamber for periods of (a) 5.0 s, (b) 7.5 s, (c) 9.0 s and (d) 12.0 s for the OWC with chamber turbine obtained by Fluinco and Fluent.

amplitude factor and phase angle in the OWC chamber, besides the pneumatic power of the device.

The results presented in this section, with open chamber and with chamber turbine, show that the aerodynamic model implemented in the Fluinco numerical code is a promising tool to model a complete OWC device, considering both hydrodynamics and aerodynamics. Besides being simple to implement, this methodology provides lower computational cost and geometric complexity, mainly due to two reasons: it is not necessary to calculate the flow variables of the air domain and the domain may be 2D, different from modeling in which the turbine and the 3D

chamber are directly modeled, requiring the use of a 3D domain, such as in the Fluent simulations.

4. Study of chamber geometry and turbine characteristic relation influences on OWC performance using Fluinco

In this section, the influence of several geometric parameters and the turbine characteristic relation on the OWC device behavior is investigated. The sequences of parameter variations are the following: on the front wall submergence depth (d), the chamber length (B), the turbine characteristic relation (kt) and the chamber

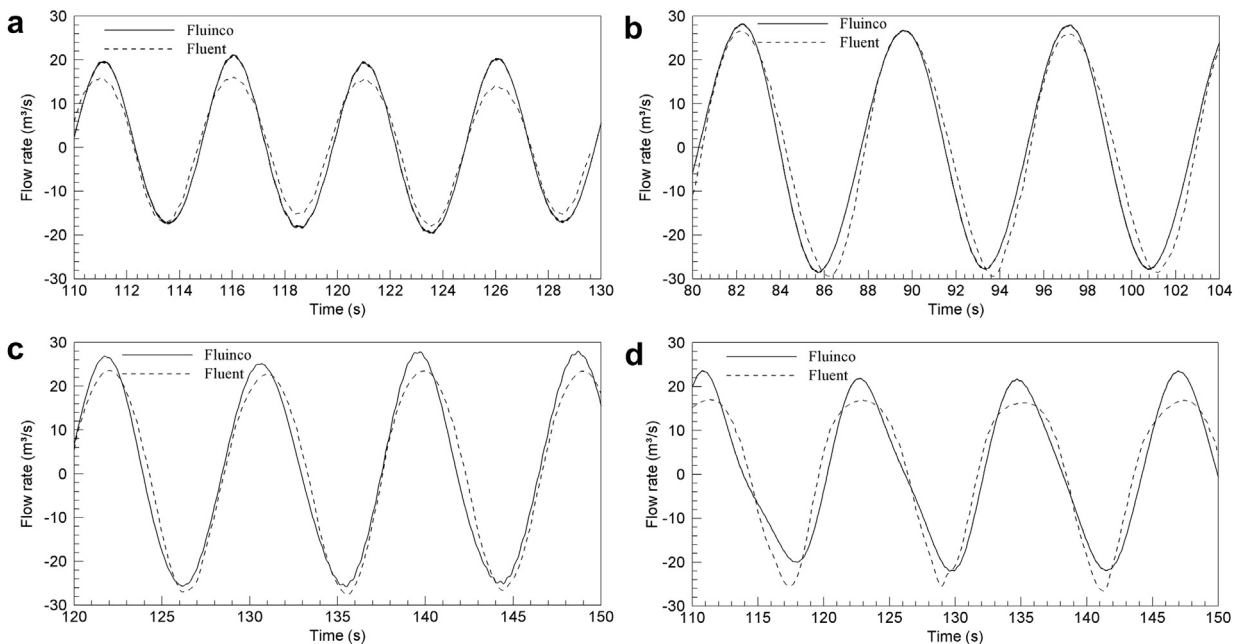


Fig. 14. Time series of the flow rate for periods of (a) 5.0 s, (b) 7.5 s, (c) 9.0 s and (d) 12.0 s for the OWC with chamber turbine obtained by Fluinco and Fluent.

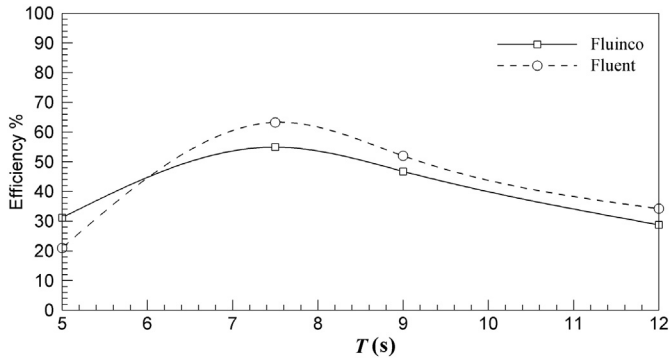


Fig. 15. Efficiency of OWC with chamber turbine obtained by Fluinco and Fluent.

height (h_c). The front wall thickness (0.5 m), the water depth ($h = 10.0$ m) and the chamber width ($D = 10.0$ m) are constants. Incident waves of periods from $T = 4.0$ – 14.0 s are simulated keeping a constant height equal to $H_0 = 1.0$ m.

4.1. Front wall depth variation

In this section, the influence of the front wall submergence depth on the pneumatic power of the OWC device is investigated. The following parameters are kept constant during simulations: $kt = 119.4 \text{ Pa m}^{-3} \text{ s}$, $B = 10.0$ m and $h_c = 6$ m.

Fig. 16 shows the efficiency of OWC obtained for front wall submergence depths of $d = 2.5$ m, 5.0 m and 7.5 m ($d/h = 1/4$, $1/2$ and $3/4$). It can be observed that the performance of the device with front wall immersion length of 2.5 m is superior for all period waves, except for $T = 14.0$ s. The efficiency with $d = 5.0$ m is similar to the one adopting $d = 2.5$ m, except for periods lower than 8.0 s in which the efficiency is lower. Efficiency for $d = 7.5$ m is the lowest one, reaching only 39% of the efficiency obtained for $d = 2.5$ m at $T = 6.0$ s.

It can be seen that the longer the front wall submergence depth, the higher the value of the period of the optimal efficiency; the optimal points are around 6.0 s ($d = 2.5$ m), 8.0 s ($d = 5.0$ m) and 9.0 s ($d = 7.5$ m) with efficiencies of 67.3%, 64.0% and 53.1%, respectively. This characteristic is explained considering that the frequency of the resonance decreases (period of the resonance increases) when the front wall submergence depth increases, because the distance that the fluid particles travel during a period also increases [20].

The minimum elevation inside the chamber, 0.75 m, is obtained for $d = 2.5$ m and $T = 14.0$ s. This value is a restriction for the minimum front wall submergence depth that may avoid the

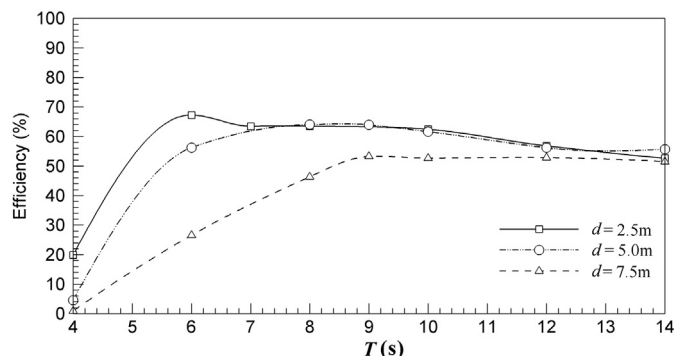


Fig. 16. Efficiency of OWC for $d = 2.5$ m, 5.0 m and 7.5 m.

entrance of air inside the chamber. Other effects must be considered to establish a safety length, such as tide and wave transformations near the installation zone of the device mainly due to the coastline topography and the bathymetry surrounding the device [23,28].

4.2. Chamber length variation

In these cases, the following parameters are fixed: $d = 2.5$ m, $kt = 119.4 \text{ Pa m}^{-3} \text{ s}$ and $h_c = 6.0$ m. Fig. 17 shows the pneumatic power obtained for chamber lengths of 5.0 m and 10.0 m. It can be observed that the performance of the device with length of 10 m is much superior for all period waves, except for $T = 4.0$ s. The optimal point is around $T = 6.0$ s for both cases, corresponding to efficiencies of 67.48% and 80.69% for $B = 5.0$ m and 10.0 m, respectively.

The air–water interaction inside the chamber is better understood analyzing time series of air pressure, free surface elevation (on a gauge in the middle position inside the chamber), air flow rate and pneumatic power, which are showed in Figs. 18 and 19 for $B = 5.0$ m and 10.0 m, respectively. The specific mass of the air is coupled to the pressure and the values vary from 1.175 kg/m^3 to 1.254 kg/m^3 (with difference around 6%). From Figs. 18 and 19 the following observations can be done:

- The air pressure, flow rate and, consequently, the pneumatic power are in phase, but they are in different phase from the free surface elevation. The phase angle between the free surface elevation and the air pressure (or flow rate or pneumatic power) varies from 80° to 50° approximately, in which the highest phase angles correspond to the lowest period.
- There is a strong non linearity in pressure and flow rate behaviors for the wave period of 14.0 s in both chambers ($B = 5.0$ m and 10.0 m), unlike the case of other lower periods. A harmonic wave can be identified in the chamber with a period $T/2$. Free surface elevation on gauge in the middle position inside the chamber shows a non-sinusoidal pattern due to harmonic waves that appear in this configuration and non-linear effects. For wave period $T = 12$ s, even if the free surface flow on this gauge presents a sinusoidal pattern, non-linear effects clearly appear in time series of pressure and flow rate.
- It can be seen that free surface elevation is not symmetric around the still water level. Wave caves (depression) are smaller than wave crests (compression) and maximum of pneumatic power is smaller for depression than compression. These differences seem to increase when the wave period increases.

Fig. 20 shows the mean amplitudes of the oscillatory movement of free surface (elevation), pressure and flow rate for both chamber lengths. It can be seen that the free surface amplitudes, for both

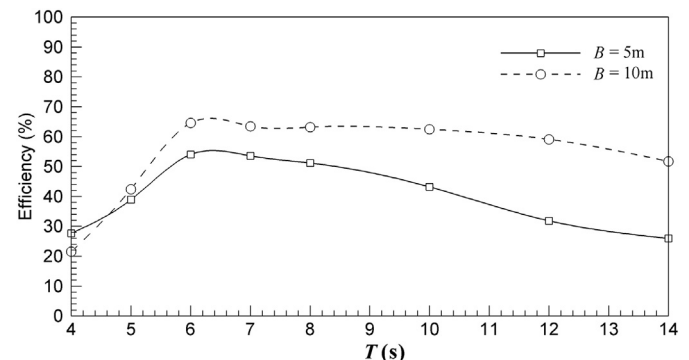


Fig. 17. Efficiency of OWC for $B = 5.0$ m and 10.0 m and $d = 2.5$ m.

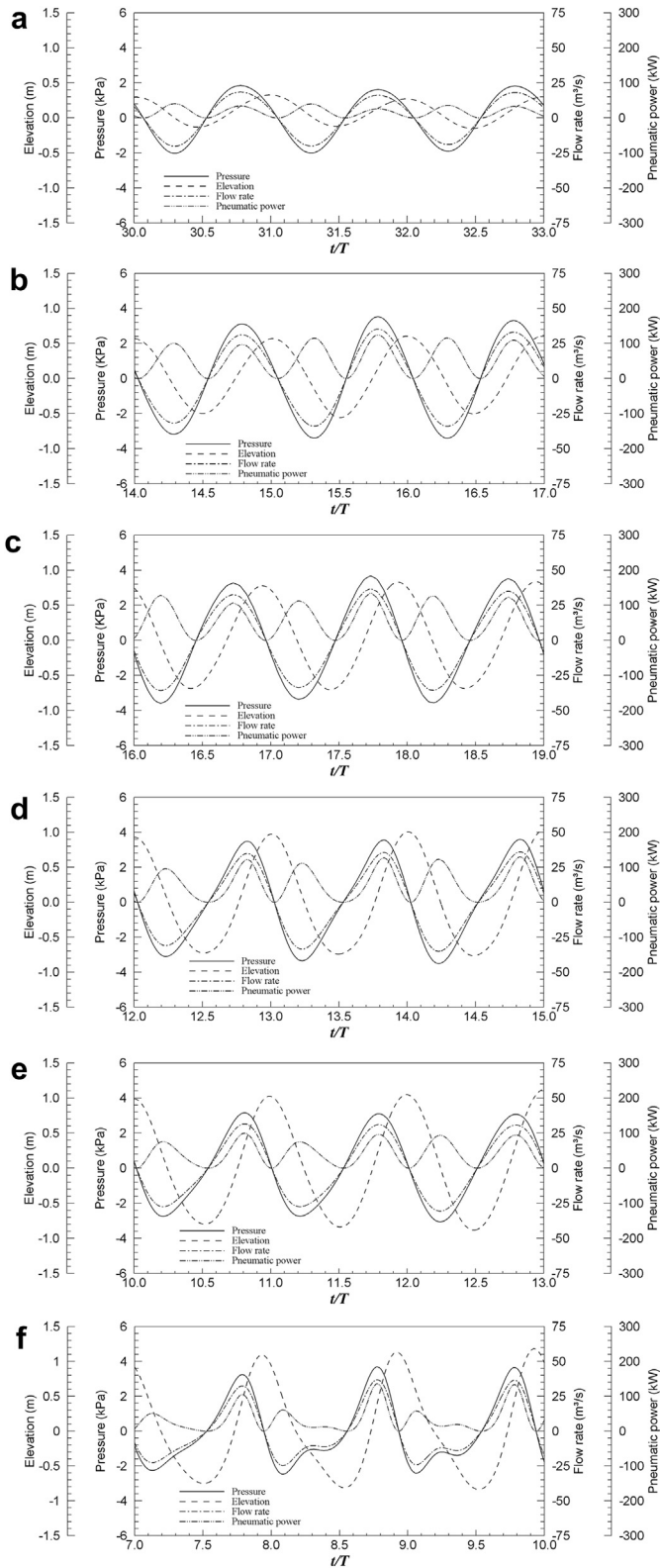


Fig. 18. Time series of air pressure, elevation, flow rate and pneumatic power for $B = 5.0$ m and wave periods of (a) 4.0 s, (b) 6.0 s, (c) 8.0 s, (d) 10.0 s, (e) 12.0 s and (f) 14.0 s.

cases, increase with the incident wave period and have a lower variation in high values. Moreover, the pressure increase up to $T = 8.0$ s and 10.0 s for chamber lengths of 5.0 m and 10.0 m, respectively, and fall smoothly to higher periods. The behavior of flow rate is similar to the pressure.

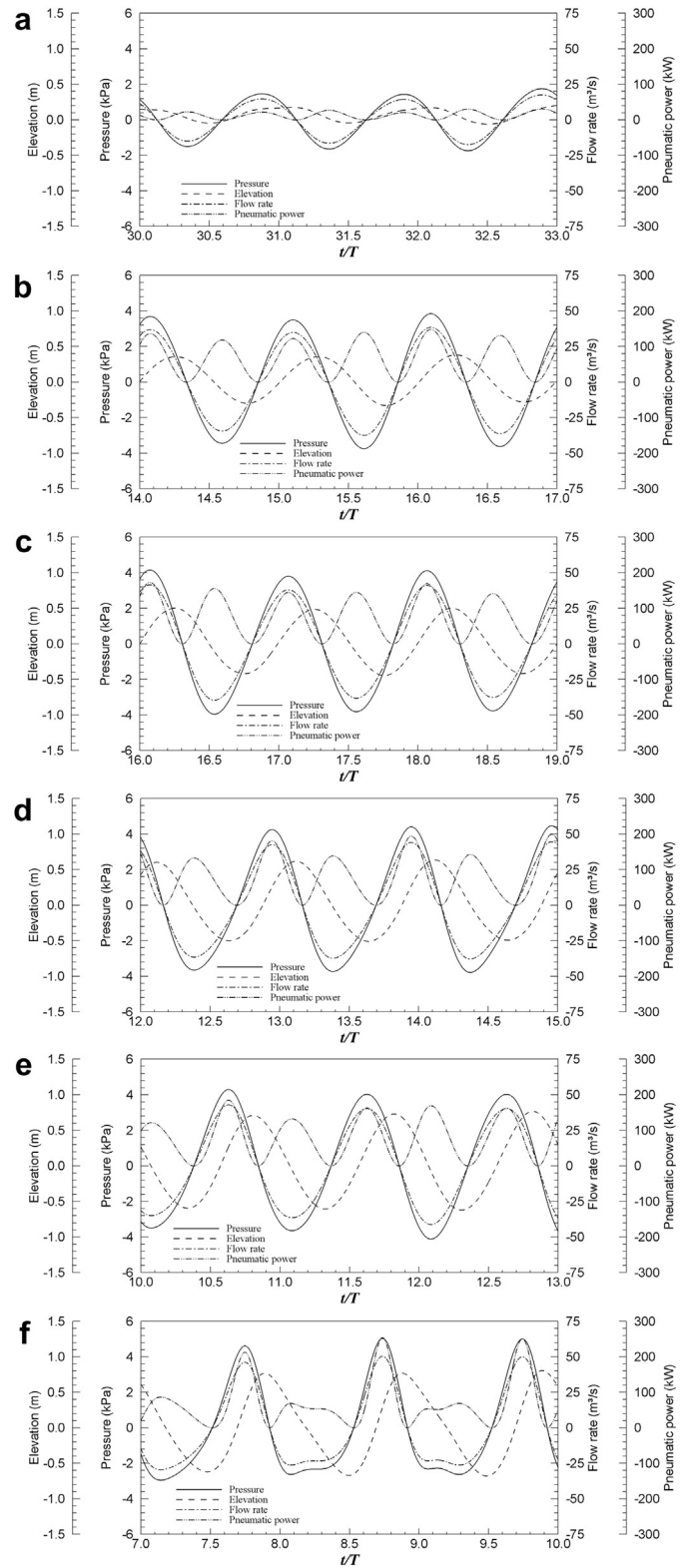


Fig. 19. Time series of air pressure, elevation, flow rate and pneumatic power for $B = 10.0$ m and wave periods of (a) 4.0 s, (b) 6.0 s, (c) 8.0 s, (d) 10.0 s, (e) 12.0 s and (f) 14.0 s.

4.3. Turbine characteristic relation variation

The analysis of the influence of the turbine characteristic relation on performance of the OWC device is carried out by using a chamber length $B = 10.0$ m and a front wall depth $d = 2.5$ m, which

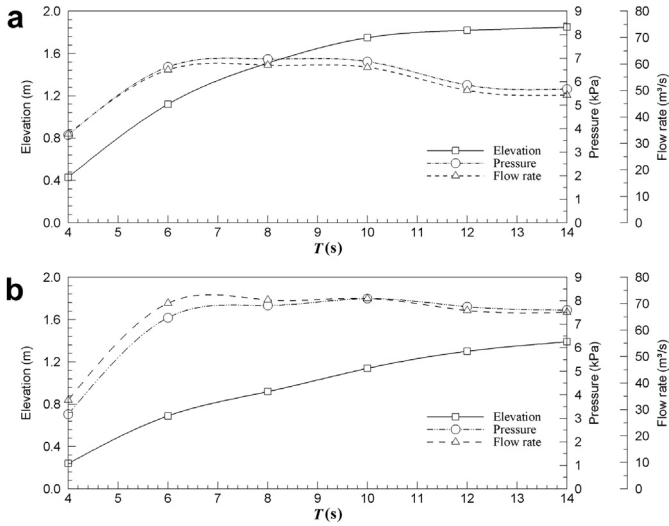


Fig. 20. Free surface elevation, pressure and flow rate amplitudes for $B = 5.0$ m (a) and $B = 10.0$ m (b).

provided better device performance in terms of efficiency, and a height chamber $hc = 6.0$ m. Fig. 21 shows the efficiency curves for kt from 40 to 230 $\text{Pa m}^{-3} \text{s}$ (Fig. 21a for kt from 40 to 119.4 $\text{Pa m}^{-3} \text{s}$ and Fig. 21b for kt from 119.4 to 230 $\text{Pa m}^{-3} \text{s}$). The behavior of the curves is similar, except for the lowest period ($T = 4$ s). It can be noticed that from $kt = 40 \text{ Pa m}^{-3} \text{s}$ to $kt = 100 \text{ Pa m}^{-3} \text{s}$, approximately, the available power to the turbine increase. It is worth emphasizing that the efficiency obtained by using $kt = 119.4 \text{ Pa m}^{-3} \text{s}$ is close to the one that adopts $kt = 100 \text{ Pa m}^{-3} \text{s}$. From $kt = 100 \text{ Pa m}^{-3} \text{s}$ to $kt = 230 \text{ Pa m}^{-3} \text{s}$, approximately, the efficiency decreases.

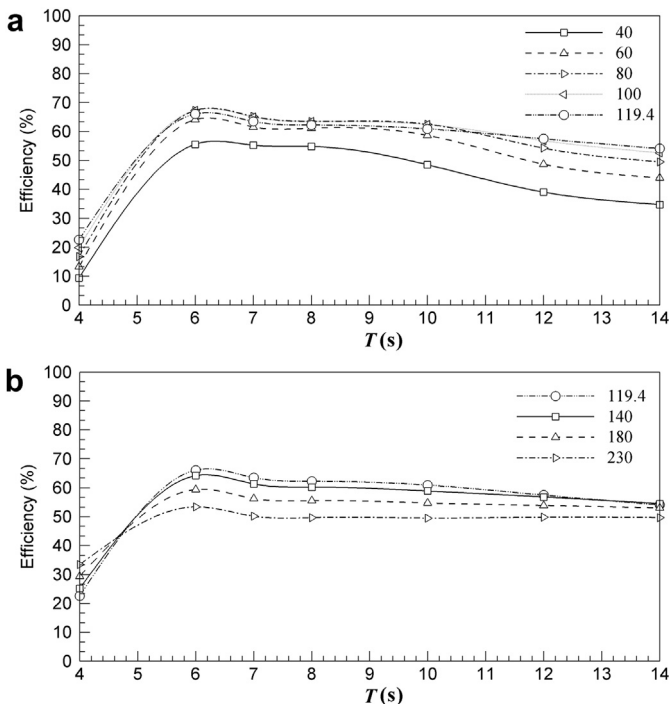


Fig. 21. Efficiencies for turbine characteristic relations from (a) $kt = 40 \text{ Pa m}^{-3} \text{s}$ to $kt = 119.4 \text{ Pa m}^{-3} \text{s}$ and (b) $kt = 119.4 \text{ Pa m}^{-3} \text{s}$ to $kt = 230 \text{ Pa m}^{-3} \text{s}$.

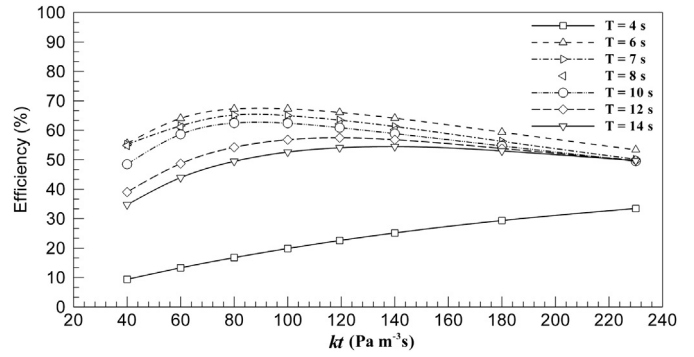


Fig. 22. Efficiency related to the turbine characteristic relations for periods from $T = 4$ s to $T = 14$ s.

Fig. 22 shows curves of the efficiency related to the turbine characteristic relation for each period. The optimal efficiencies occur for $T = 6.0$ s for all turbine characteristic relation curves; this fact indicates that the variation of kt does not affect the optimal efficiency point of the device. It may also be noticed that, for periods between 6 s and 10 s, the optimal efficiency occurs for kt from 80 $\text{Pa m}^{-3} \text{s}$ to 100 $\text{Pa m}^{-3} \text{s}$, approximately, and, for periods between 12 s and 14 s, the optimal efficiency occurs for kt from 120 $\text{Pa m}^{-3} \text{s}$ to 140 $\text{Pa m}^{-3} \text{s}$, approximately. Therefore, this system behavior shows that the characteristic of the device must be adapted, according to the wave climate of the region where it will be installed.

These variation can be better understand analyzing Fig. 23, which shows time series of free surface elevation, pressure, flow rate and pneumatic power for wave period of 10.0 s and $kt = 40, 100$ and 230 $\text{Pa m}^{-3} \text{s}$. For $kt = 40 \text{ Pa m}^{-3} \text{s}$, the maximum amplitude of the elevation is high (around 0.9 m), the maximum amplitude of the pressure is low (2.0 kPa) and the flow rate is very high (52 m^3/s). For $kt = 230 \text{ Pa m}^{-3} \text{s}$, the maximum amplitude of the elevation is low (0.4 m), the maximum amplitude of the pressure is very high (5.2 kPa) and the flow rate is low (20 m^3/s). Therefore, as kt increases, the pressure in the chamber also increases but the flow rate decreases. Thus, there is an optimal situation, which, in this case, occurs at $kt = 100 \text{ Pa m}^{-3} \text{s}$, as shown in Fig. 23c. This fact indicates a compromise between the pressure and the flow rate with the optimum efficiency.

4.4. Chamber height variation

The influence of the air volume of the chamber on the device performance is analyzed by varying the chamber height ($hc = 4.0$ m, 6.0 m and 8.0 m) in a range of wave periods (from 4.0 s to 14.0 s). In these cases, the other parameters $d = 2.5$ m, $kt = 100 \text{ Pa m}^{-3} \text{s}$ and $B = 10.0$ m are kept constant. Fig. 24 shows the efficiency curve for each chamber height. As the height hc decreases, the efficiency increases for every wave periods, in a smooth way. This tendency indicates that the best value of hc is the lowest one. However, its limit is when the water reaches the entry of the turbine system. Since the maximum elevation inside the chamber is 0.95 m (for $hc = 4.0$ m and $T = 14.0$ s), it can be concluded that the chamber height must be higher than this value in order to take into account other possible effects, such as tidal and local wave transformations.

5. Conclusions

A study of the aerodynamic and hydrodynamic flows and performance of an onshore OWC energy extraction device, using

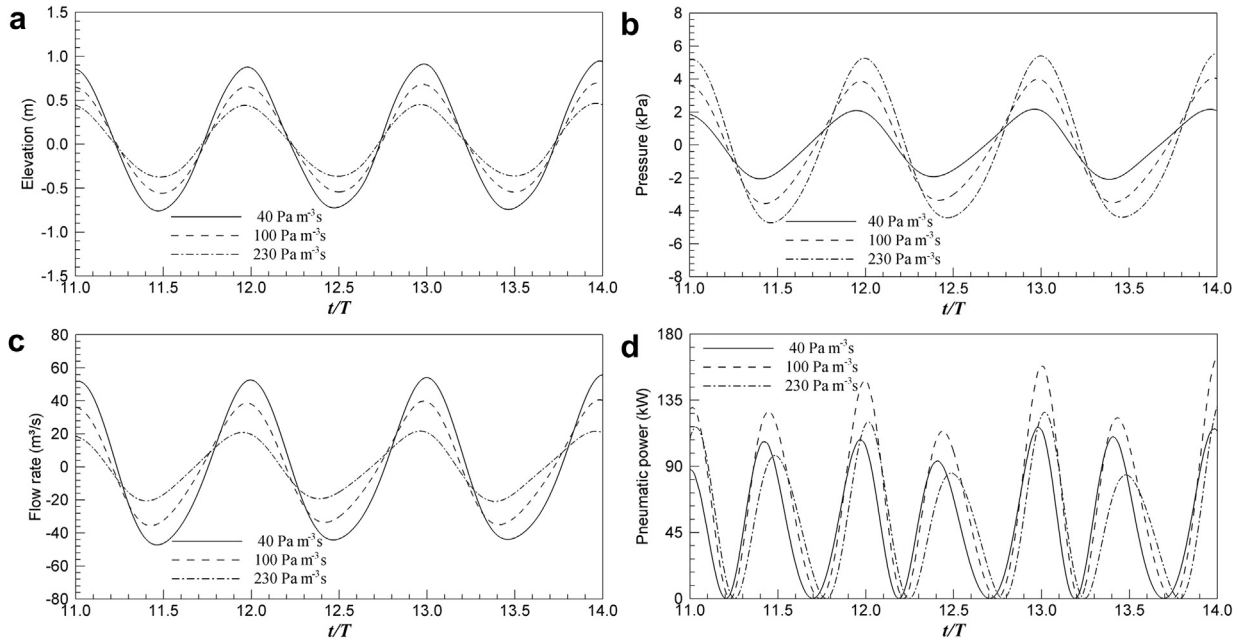


Fig. 23. Free surface elevation (a), air pressure (b), flow rate (c) and pneumatic power (d) for wave period $T = 10.0$ s and $kt = 40, 100$ and $230 \text{ Pa m}^{-3} \text{ s}$.

Fluinco, a numerical model based on Navier–Stokes equations, is presented in this paper. Fluinco is a code based on semi-implicit two-step Taylor–Galerkin method and an ALE formulation to enable the solution of problems involving movements of free surface. An aerodynamic model based on the first principle of thermodynamics is implemented, taking into account the effect of a Wells turbine.

Firstly, in order to validate the Fluinco code, results are compared to those obtained by Fluent commercial numerical code for an OWC device with an open chamber and a chamber with a turbine. The first study case (open chamber) consists of the simulation of incident regular waves, with wave height of 1.0 m and wave period from 5.0 s to 18.0 s, on onshore OWC device with a 10 m long open chamber and a 0.5 m thick front wall and submergence depth of 5 m. The amplification factor and the phase angle obtained by both models are very similar. The sloshing parameter, which quantifies the magnitude of the sloshing inside the chamber, presents the same behavior for both models: larger values for periods lower than 7.5 s and lower values for periods of 9.0 s; between these periods, there is high variation. Fluent systematically presents lower values than Fluinco. The second study

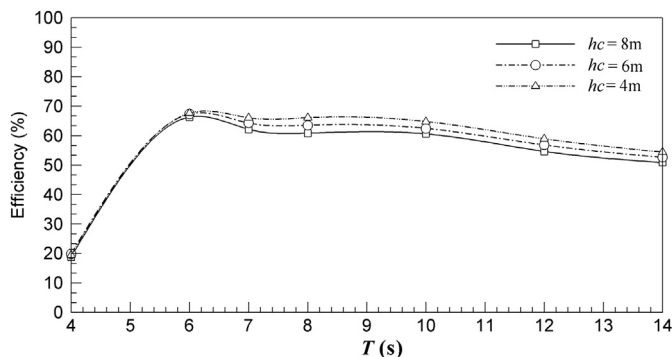


Fig. 24. Efficiency of OWC with chamber height variation for $d = 2.5$ m, $kt = 100 \text{ Pa m}^{-3} \text{ s}$ and $B = 10.0$ m.

case (chamber with a turbine) consists of a 10.0 m deep flume with a 5.0 m long chamber in its end. The frontal wall is 0.5 m thick and $d = 5.0$ m deep. The width of the chamber is 8.0 m and the height in relation to the mean water level is 10.0 m. A Wells turbine is considered with a characteristic relation equal to $kt = 0.120 \text{ Pa m}^{-3} \text{ s}$, which is very similar to the one used in the European pilot plant built on the Pico island, Azores (Portugal) ($kt = 119.4 \text{ Pa m}^{-3} \text{ s}$). Air-duct diameter is 1.0 m and its axis is located 8.5 m above the free surface at rest. Incident regular waves with periods from 5.0 s to 12.0 s and 1.0 m height are simulated. Time series of the air pressure and the flow rate obtained by both models show good agreement; some non-linear behavior in negative values of the pressure presented by Fluent do not occur when Fluinco is used. The behavior of the pneumatic power for this case obtained by both two models is similar, with a 13% difference between Fluinco and Fluent for wave period 7.5 s, with a value of pneumatic power obtained by Fluinco slightly lower than that of Fluent which systematically presents larger values by comparison with Fluinco.

The results obtained by Fluinco are in very good agreement with those obtained by Fluent for two configurations of the OWC chamber, with open chamber and with chamber turbine, in terms of free surface levels, amplification factor and phase angle in the OWC chamber, besides the pneumatic power of the device, even if both codes, based on the Navier–Stokes equations, use two very different numerical approaches for discretization of equations, for free surface modeling and for aerodynamic modeling in the OWC chamber.

After these comparisons between Fluinco and Fluent, the former is applied to analyze the influence of the chamber geometry and the turbine characteristic relation in the device performance, measured in terms of pneumatic power. During the investigation, the depth (10.0 m), thickness of the front wall (0.5 m) and the wave height (1.0 m) are kept constant. Afterwards, the influence of front wall depth, chamber length, turbine characteristic relation and chamber height, considering, in each step, optimal values previously obtained, is analyzed. As a result, the front wall depth equal to 2.5 m reaches the best performance in terms of pneumatic power,

although, between 2.5 m and 5.0 m, little variation is found. The chamber length of 10.0 m provides the optimal pneumatic power. The influence of the turbine characteristic relation is analyzed for values varying from $40 \text{ Pa m}^{-3} \text{ s}$ to $230 \text{ Pa m}^{-3} \text{ s}$, using a chamber length of 10.0 m and a front wall depth of 2.5 m. The turbine characteristic relation with the best performance varies according to the wave period: $80 \text{ Pa m}^{-3} \text{ s}$ to $100 \text{ Pa m}^{-3} \text{ s}$ for periods between 6 s and 10 s and $120 \text{ Pa m}^{-3} \text{ s}$ to $140 \text{ Pa m}^{-3} \text{ s}$ for periods between 12 s and 14 s. Finally, the chamber height tests indicate little influence over the device performance. As a result, the adequate height is the lowest one that allows the turbine operation.

The results obtained for an OWC device with open chamber and with chamber turbine show that the aerodynamic model implemented in the Fluinco numerical code is a promising tool for modeling a complete OWC device, considering both hydrodynamics and aerodynamics.

Acknowledgments

The authors acknowledge the support of CNPq (project 303308/2009-5) and CAPES for the post-graduate scholarship.

References

- [1] Pontes MT, Falcão AFO. Oceans energies: recourses and utilization. In: Proceedings of the 18th world energy conference, Buenos Aires 2001.
- [2] Beyene A, Wilson JH. Comparison of wave energy flux for northern, central, and southern coast of California based on long-term statistical wave data. *Energy* 2006;31:1856–69.
- [3] Iglesias G, Carballo R. Wave energy potential along the Death Coast (Spain). *Energy* 2009;34:1963–75.
- [4] Kim G, Jeong WM, Lee KS, Jun K, Lee ME. Offshore and nearshore wave energy assessment around the Korean Peninsula. *Energy* 2011;36:1460–9.
- [5] Akpınar A, Kömürçü Mİ. Wave energy potential along the south-east coasts of the Black Sea. *Energy* 2012;42:289–302.
- [6] Mollison D, Pontes MT. Assessing the Portuguese wave-power resource. *Energy* 1992;17:255–68.
- [7] Masuda Y, McCormick ME. Experiences in pneumatic wave energy conversion in Japan. In: McCormick ME, Kim YC, editors. Utilization of ocean waves-wave to energy conversion ASCE, New York 1987. p. 1–33.
- [8] Falcão AFO. Wave energy utilization: a review of the technologies. *Renew Sustain Energy Rev* 2010;14:899–918.
- [9] Barreiro TG, Gil L. Energia das ondas marítimas: tecnologias e a experiência portuguesa. *Anais do Clube Militar Naval* 2008;CXXXVIII:403–22 [in Portuguese].
- [10] Falcão AFO. The development of wave energy utilization. International energy agency implementing agreement on ocean energy systems; 2008. Annual Report.
- [11] McCormick ME. A modified linear analysis of a wave-energy conversion buoy. *Ocean Eng* 1976;3:133–44.
- [12] Evans DV. A theory for wave power absorption by oscillating bodies. *J Fluid Mech* 1976;77:1–25.
- [13] Mei CC. Power extraction from water waves. *J Ship Res* 1976;20:63–6.
- [14] Newman JN. The interaction of stationary vessels with regular waves. In: Proceedings of the 11th symposium on naval hydrodynamics, London 1976. p. 491–501.
- [15] Budal K, Falnes J. Optimum operation of improved wave-power converters. *Marine Sci Commun* 1977;3:133–50.
- [16] Evans DV. The oscillating water column wave-energy device. *J Inst Math Appl* 1978;22:423–33.
- [17] Falcão AFO, Sarmento AJNA. Wave generation by a periodic surface pressure and its application in wave-energy extraction. In: 15th international congress of theoretical and applied mechanics, Toronto 1980.
- [18] Evans DV. Wave-power absorption by systems of oscillating surface pressure distributions. *J Fluid Mech* 1982;114:481–99.
- [19] Falnes J, McIver P. Surface wave interactions with systems of oscillating bodies and pressure distributions. *Applied Ocean Res* 1985;7:225–34.
- [20] Evans DV, Porter R. Hydrodynamic characteristics of an oscillating water column device. *Applied Ocean Res* 1995;17:155–64.
- [21] Count BM, Evans DV. The influence of projecting sidewalls on the hydrodynamic performance of wave-energy devices. *J Fluid Mech* 1984;145:361–76.
- [22] You Ya-ge. Hydrodynamic analysis on wave power devices in near-shore zones. *J Hydrodyn* 1993;3(B5):42–54.
- [23] You Y, Yu Z, Katory M, Li Y. Onshore wave power stations: analytical and experimental investigations. In: Proceedings of the 16th international conference on Offshore mechanics and Arctic engineering, Yokohama 1997. p. 105–12.
- [24] Lee CH, Newman JN, Nielsen FG. Wave interactions with an oscillating water column. In: Proceedings of the 6th international Offshore and Polar engineering conference, Los Angeles 1996. p. 82–90.
- [25] Brito-Melo A, Sarmento AJNA, Clément AH, Delhommeau GA. 3D boundary element code for analysis of OWC wave-power plants. In: Proceedings of the ninth international Offshore and Polar engineering conference, Brest 1999. p. 188–95.
- [26] Delauré YMC, Lewis A. 3D hydrodynamic modeling of fixed oscillating water column wave power plant by a boundary element methods. *Ocean Eng* 2003;30:309–30.
- [27] Clément AH. Dynamic nonlinear response of OWC wave energy devices. *Int J Offshore Polar Eng* 1997;7(2):154–9.
- [28] Wang DJ, Katory M, Li YS. Analytical and experimental investigation on the hydrodynamic performance of onshore wave-power devices. *Ocean Eng* 2002;29:871–85.
- [29] Lopes MFP, Ricci P, Gato LMC, Falcão AFO. Experimental and numerical analysis of the oscillating water column inside a surface-piercing vertical cylinder in regular waves. In: Proceedings of the 7th European wave and tidal energy conference, Porto 2007.
- [30] WAMIT manual V.6.2 PCwww.wamit.com; 2004.
- [31] Josset C, Clément AH. A time-domain numerical simulator for oscillating water column wave power plants. *Renew Energy* 2007;32:1379–402.
- [32] Alves MA, Costa IR, Sarmento AJNA, Chozas JF. Performance evaluation of an axisymmetric floating OWC. In: Proceedings of the 20th international Offshore and Polar engineering conference, Beijing 2010.
- [33] Horiko M. CFD optimization of an oscillating water column wave energy converter. Degree of master of engineering science, School of mechanical engineering, Faculty of engineering, computing and mathematics. The University of Western Australia; 2007.
- [34] Liu Z, Hyun BS, Hong KY. Application of numerical wave tank to OWC air chamber for wave energy conversion. In: Proceedings of the 18th international Offshore and Polar engineering conference, Vancouver 2008. p. 350–6.
- [35] Marjani AE, Ruiz FC, Rodriguez MA, Santos MTP. Numerical modelling in wave energy conversion systems. *Energy* 2008;33:1246–53.
- [36] Liu Z, Shi H, Hyun B. Practical design and investigation of the breakwater OWC facility in China. In: Proceedings of the 8th European wave and tidal energy conference, Uppsala 2009.
- [37] Liu Z, Hyun B, Hong K, Lee Y. Investigation on integrated system of chamber and turbine for OWC wave energy converter. In: Proceedings of the nineteenth international Offshore and Polar engineering conference, Osaka 2009.
- [38] Clément A, Babarit A, Gilloteaux JC, Josset C, Duclos G. The SEAREV wave energy converter. In: Proceedings of the 6th European wave and tidal energy conference, Glasgow 2005.
- [39] McCabe AP, Aggidis GA, Widden MB. Optimizing the shape of a surge-and-pitch wave energy collector using a genetic algorithm. *Renew Energy* 2010;35(12):2767–75.
- [40] Gomes RPF, Henriques JCC, Gato LMC, Falcão AFO. IPS 2-body wave energy converter: acceleration tube optimization. *Int J Offshore Polar Eng* 2010;20(4):247–55.
- [41] Teixeira PRF, Awruch AM. Numerical simulation of fluid-structure interaction using the finite element method. *Comput Fluids* 2005;34:249–73.
- [42] Teixeira PRF, Popiolek TL, Vanini L. Numerical analysis of three-dimensional free surface flows using adaptive meshes. In: Proceedings of the 28th Iberian Latin american congress on computational methods in engineering, Porto 2007.
- [43] Teixeira PRF, Fortes CJEM. Aplicação de um modelo numérico não-linear tridimensional na análise de ondas sobre quebra-mares trapezoidais submersos. *Revista Internacional de Métodos Numéricos para Cálculo y Diseño en Ingeniería* 2009;25(4):313–36.
- [44] Paixão Conde JM, Teixeira PRF, Didier E. Numerical simulation of an oscillating water column wave energy converter: comparison of two numerical codes. In: Proceedings of the 21th international Offshore and Polar engineering conference 2011. p. 668–74.
- [45] Didier E, Paixão Conde JM, Teixeira PRF. Numerical simulation of an oscillation water column wave energy converter with and without damping. In: Proceedings of the fourth international conference on computational methods in marine engineering, Lisbon 2011. p. 206–17.
- [46] Teixeira PRF, Awruch AM. Three-dimensional simulation of high compressible flows using a multi-time-step integration technique with subcycles. *Appl Math Model* 2001;25:613–27.
- [47] Argyris J, St Doltsinis J, Wuestenberg H, Pimenta PM. Finite element solution of viscous flow problems, finite elements in fluids, vol. 6. New York: Wiley-Interscience; 1985. p. 89–114.
- [48] Löhner R, Morgan K, Zienkiewicz OC. An adaptive finite element procedure for compressible high speed flows. *Comp Meth Appl Mech Eng* 1985;51:441–65.
- [49] Ramaswamy R, Kawahara M. Arbitrary lagrangian-eulerian finite element method for unsteady, convective, incompressible viscous free surface fluid flow. *Int J Numerical Meth Fluids* 1987;7:1053–75.
- [50] Falcão AFO, Justino PAP. OWC wave energy devices with air flow control. *Ocean Eng* 1999;26:1275–95.
- [51] Brito-Melo A, Gato LMC, Sarmento AJNA. Analysis of wells turbine design parameters by numerical simulation of the OWC performance. *Ocean Eng* 2002;29:1463–77.
- [52] Dean RG, Dalrymple RA. Water wave mechanics for engineers and scientists, advanced series on ocean engineering, vol. 2. World Scientific; 1991.
- [53] ANSYS FLUENT 6.3 user's guide. Fluent Inc; 2006.

- [54] Hirt CW, Nichols BD. Volume of fluid (VoF) method for the dynamics of free boundaries. *J Comp Physiol* 1981;39:201–25.
- [55] Peric M, Ferziger JH. *Computational methods for fluid dynamics*. 2nd ed. Berlin: Springer; 1997.
- [56] Barreiro T, Didier E, Gil L, Alves M. Simulação numérica não linear do escoamento gerado pela interação entre a agitação marítima e conversores pontuais de energia das ondas. In: *Conferência Nacional em Mecânica de Fluidos, Termodinâmica e Energia, Bragança 2009* [in Portuguese].
- [57] Morris-Thomas MT, Irvin RJ, Thiagarajan KP. An investigation into the hydrodynamic efficiency of an oscillating water column. *J Offshore Mechanics Arctic Eng* 2007;129:273–8.
- [58] Thakker A, Dhanasekaran TS, Takao M, Setoguchi T. Effects of compressibility on the performance of a wave-energy conversion device with an impulse turbine using a numerical simulation technique. *Int J Rotating Machinery* 2003;9:443–50.